

THE CRONOS CODE FOR ASTROPHYSICAL MAGNETOHYDRODYNAMICS

R. KISSMANN¹, J. KLEIMANN², B. KREBL¹, AND T. WIENGARTEN²

¹Institut für Astro- und Teilchenphysik, Universität Innsbruck, Austria

²Institut für Theoretische Physik IV, Ruhr-Universität Bochum, Germany

Draft version July 4, 2018

ABSTRACT

We describe the magnetohydrodynamics (MHD) code CRONOS, which has been used in astrophysics and space-physics studies in recent years. CRONOS has been designed to be easily adaptable to the problem in hand, where the user can expand or exchange core modules or add new functionality to the code. This modularity comes about through its implementation using a C++ class structure. The core components of the code include solvers for both hydrodynamical (HD) and MHD problems. These problems are solved on different rectangular grids, which currently support Cartesian, spherical, and cylindrical coordinates. CRONOS uses a finite-volume description with different approximate Riemann solvers that can be chosen at runtime. Here, we describe the implementation of the code with a view toward its ongoing development. We illustrate the code's potential by several (M)HD test problems and some astrophysical applications.

Keywords: hydrodynamics — magnetohydrodynamics (MHD) — methods: numerical

1. INTRODUCTION

Many problems in astrophysics and space physics require the use of numerical methods – especially for cases where a direct comparison to observations is desired. This applies particularly to environments that can be described with the help of fluid dynamics. The CRONOS code that is described here has already been applied to several research problems in space physics and astrophysics.

There is quite a range of codes available for the solution of hydrodynamics (HD) or magnetohydrodynamics (MHD) problems. This includes – but is not limited to – ATHENA (Stone et al. 2008; Skinner & Ostriker 2010), AMRVAC (van der Holst et al. 2008; Keppens et al. 2012; van der Holst et al. 2012), RACOON (Dreher & Grauer 2005), RAMSES (Teyssier 2002; Fromang et al. 2006), NIRVANA (Ziegler 2008, 2011a,b), PLUTO (Mignone et al. 2007, 2012), and ZEUS (Stone & Norman 1992a,b). Thus, it might seem questionable whether introducing yet another code is necessary. Each of the above codes, however, has been developed with some focus in mind, thus leading to sometimes considerable differences in implementation and available features.

For CRONOS, the focus during the development of the code was on easy adaptability for additional aspects needed in specific astrophysical modeling efforts. Apart from that, CRONOS is not only limited to the solution of the (M)HD equations, but also allows additional conservation laws, which are to be provided by the user, to be solved. A frequently used option is to include tracer fields, but in principle many other conservation laws, such as for instance transport equations, can be treated as well.

CRONOS was developed with applications from the fields of astrophysics and space physics in mind. Typical applications comprise simulations of turbulence in the ISM (Kissmann et al. 2008; Wisniewski et al. 2012) and in magnetized accretion disks (Flaig et al. 2009, 2010, 2012), simulations of the (turbulent) solar wind and its transients (Wiengarten et al. 2013, 2014, 2015, 2016; Dalakishvili et al. 2011; Czechowski

& Kleimann 2017), applications to the heliosphere and astrospheres (Scherer et al. 2015; Röken et al. 2015; Scherer et al. 2016a,b; Kleimann et al. 2017), and investigations of high-energy particle acceleration in colliding-wind binary systems (Reitberger et al. 2014b,a; Kissmann et al. 2016). Both Wiengarten et al. (2015, 2016) and Reitberger et al. (2014b) heavily relied on the option to solve additional conservation laws to model turbulence in the solar wind and additional particle species, respectively.

The code is easily usable for (M)HD problems and is continuously enhanced. The most recent addition is a multifluid prescription that is presented and verified here. Currently, the possibility of using logically rectangular grids (see, e.g. Calhoun et al. 2008), for which we will also show first results, is being implemented. CRONOS is written in the C++ programming language to allow easy extensibility. The code can either be run on a single processor or in parallel, employing the Message Passing Interface (MPI) library in the latter case. In the following, we will detail the specific implementation and the features of CRONOS. Correspondingly, this manuscript will serve as a reference for users of the code.

2. SYSTEM OF EQUATIONS

The CRONOS code was developed to solve systems of hyperbolic conservation laws of the general form

$$\frac{\partial \mathbf{w}}{\partial t} + \nabla \cdot \mathbf{F}(\mathbf{w}, \mathbf{r}, t) = \mathbf{s}, \quad (1)$$

where \mathbf{w} is the density relating to a conserved quantity, \mathbf{F} is the corresponding flux function, and \mathbf{s} is an optional source term. The main solvers allow for the solution of the systems of equations of both HD and MHD, with the option to add and solve user-defined conservation laws. In the following, we will focus on the solution of the MHD equations, since the HD solver internally represents a sub-part of the MHD solver.

In the context of MHD, CRONOS solves the following set

of partial differential equations (PDEs):

$$\frac{\partial n}{\partial t} + \nabla \cdot (n\mathbf{u}) = 0, \quad (2)$$

$$\frac{\partial (mn\mathbf{u})}{\partial t} + \nabla \cdot (mn\mathbf{u}\mathbf{u}) + \nabla p + \frac{1}{\mu_0}\mathbf{B} \times (\nabla \times \mathbf{B}) = \mathbf{f}, \quad (3)$$

$$\frac{\partial \mathbf{B}}{\partial t} = -\nabla \times \mathbf{E} = \nabla \times (\mathbf{u} \times \mathbf{B}), \quad (4)$$

$$\frac{\partial e}{\partial t} + \nabla \cdot \left[\left(e + \frac{B^2}{2\mu_0} + p \right) \mathbf{u} - \frac{1}{\mu_0} (\mathbf{u} \cdot \mathbf{B}) \mathbf{B} \right] = \mathbf{u} \cdot \mathbf{f}, \quad (5)$$

where the dynamical variables are the number density n , the momentum density $mn\mathbf{u}$ (with m the particle mass and \mathbf{u} the fluid velocity), the magnetic induction \mathbf{B} , and the overall energy density

$$e = e_{\text{th}} + \frac{1}{2}mn\mathbf{u}^2 + \frac{1}{2\mu_0}\mathbf{B}^2, \quad (6)$$

with μ_0 the vacuum permeability. Here, $e_{\text{th}} = p/(\gamma - 1)$ is the thermal energy density (with the adiabatic index γ), \mathbf{E} is the electric field, \mathbf{f} is some additional force density, and p is the thermal pressure.

Instead of numerically solving the energy equation (5), it is also possible to use a polytropic equation of state of the form $p = p(n)$, where two common equations of this form are implemented within CRONOS: the isothermal equation of state $p = c_s^2 mn$, with c_s the isothermal speed of sound, or the more general form $p \propto n^\gamma$. CRONOS contains dedicated solvers for each regime (HD or MHD and full energy equation versus polytropic equation of state). The technical approach, however, is similar in each case.

2.1. Additional Equations

CRONOS provides the option to solve additional user-defined conservation laws alongside the systems of HD or MHD equations. In this case, the flux functions \mathbf{F} , which can also depend on the (M)HD variables, need to be prescribed by the user. Via the user-prescribed source term \mathbf{s} , an interaction between the different variables can also be implemented. In this context, the flux function for a passive tracer field is already implemented in CRONOS. Transport of a passive tracer can be described via the equation

$$\frac{\partial \Phi}{\partial t} + \mathbf{u} \cdot \nabla \Phi = 0. \quad (7)$$

Since this is not of conservative form, a new conserved quantity $h = \Phi n$ needs to be introduced. Combining Equations (2) and (7) yields a conservative equation for h ,

$$\frac{\partial h}{\partial t} + \nabla \cdot (h\mathbf{u}) = 0, \quad (8)$$

with $\mathbf{F}_h = h\mathbf{u}$. CRONOS allows for the use of an arbitrary number of such tracer equations. For example, Reitberger et al. (2014b) used 200 such tracer fields to simulate particles at different energies transported passively with the plasma flow. These authors additionally implemented a solver for a transport equation in energy, thus solving a four-dimensional transport equation for the energetic particles. This was realized by using the capability to implement additional user-defined PDE solvers via temporal splitting as is also foreseen within CRONOS.

In principle, the user can implement arbitrary flux functions. However, care must be taken in this case, since user-defined conservation laws are currently solved using the HLL Riemann solver (see Section 6.2.3) with the fastest signal speeds taken from the (M)HD equations. Thus, there is the danger of producing some internal inconsistency.

2.2. Multifluid flow

Recently, CRONOS was extended to allow for a multifluid description of a plasma, i.e., a description where the plasma is composed of several fluids that may or may not interact with each other and/or the magnetic field. Each fluid is described by its own set of variable fields $\{n, \mathbf{u}, e_{\text{th}}\}$, which are treated independently by simultaneously solving a separate set of Equations (2)–(5). For multifluid MHD, exactly one of these fluids is singled out as a plasma fluid experiencing magnetic field interaction, and it is this fluid's velocity that enters into the induction equation. All other fluids are treated as unmagnetized. The possible interaction of the different fluids can be implemented by prescribing the relevant source terms \mathbf{s} and has to be performed by the user. In particular, processes like photoionization or charge exchange can conveniently be realized through suitably chosen source terms for the continuity equations. The concept is illustrated in the test example of Section 8.3. Currently, no modifications to the induction equation (such as the Hall term or magnetic resistivity) have been implemented. In the following discussion, we focus on the case of single-fluid MHD, from which the treatment of all other cases can be easily inferred.

2.3. Normalization

Internally, CRONOS uses normalized units for all quantities, i.e., all variables $X = X_0 \hat{X}$ are given as the product of a normalization constant X_0 chosen by the user and a unit-free normalized variable \hat{X} that is evolved within the numerical solver. To specify the normalization, the user selects four independent normalization constants. Usually these are a length scale l_0 , a particle mass m_0 , a typical number density n_0 , and either a typical temperature T_0 or a typical value for the magnetic induction B_0 . From this, all other normalization constants are then computed via physical relations. For example, the normalization constant for the velocity is either given by the isothermal speed of sound computed from the independent normalization constants or by the Alfvén speed if the magnetic induction is used as one of the independent normalization constants. If T_0 is used as an independent normalization constant, the normalization constant for the magnetic induction is given by

$$B_0 = \sqrt{\mu_0 n_0 k_B T_0}, \quad (9)$$

where k_B is the Boltzmann constant. When applying the normalization to the system of Equations (2)–(5), all normaliza-

tion constants cancel, and we end up with

$$\frac{\partial \hat{n}}{\partial \hat{t}} + \hat{\nabla} \cdot (\hat{n} \hat{\mathbf{u}}) = 0, \quad (10)$$

$$\frac{\partial (\hat{n} \hat{\mathbf{u}})}{\partial \hat{t}} + \hat{\nabla} \cdot (\hat{n} \hat{\mathbf{u}} \hat{\mathbf{u}}) + \hat{\nabla} \hat{p} + \hat{\mathbf{B}} \times (\hat{\nabla} \times \hat{\mathbf{B}}) = \hat{\mathbf{f}}, \quad (11)$$

$$\frac{\partial \hat{\mathbf{B}}}{\partial \hat{t}} = -\hat{\nabla} \times \hat{\mathbf{E}} = \hat{\nabla} \times (\hat{\mathbf{u}} \times \hat{\mathbf{B}}), \quad (12)$$

$$\frac{\partial \hat{e}}{\partial \hat{t}} + \hat{\nabla} \cdot \left[(\hat{e} + \hat{B}^2/2 + \hat{p}) \hat{\mathbf{u}} - (\hat{\mathbf{u}} \cdot \hat{\mathbf{B}}) \hat{\mathbf{B}} \right] = \hat{\mathbf{u}} \cdot \hat{\mathbf{f}}, \quad (13)$$

where $\hat{\nabla}$ is the spatial derivative with respect to the normalized position vector $\hat{\mathbf{r}}$. Internally, CRONOS works with Equations (10)–(13), but the normalization constants are stored with the simulation data, allowing the results to be computed in physical units. To change the independent normalization constants, CRONOS supplies a pre-arranged normalization class that contains all normalization constants X_0 . This also supplies an internal means to change between physical and normalized quantities. For the remainder of this paper, the notation in Equations (10)–(13) will be used for the sake of brevity, where normalized variables will be designated as X instead of \hat{X} .

3. NOTATION AND COORDINATE SYSTEMS

3.1. Scaled Coordinates

CRONOS allows the use of any three-dimensional (3D) orthogonal coordinate system, where Cartesian (x, y, z) , cylindrical (ρ, φ, z) , and spherical (r, ϑ, φ) coordinates are currently implemented. In the standard linear case, all N_c cells of a grid extending from x_b^c to x_e^c in a given direction have the same constant extent $\Delta x^c = (x_e^c - x_b^c)/N_c$ in coordinate space, such that

$$x_i^c = x_0^c + i \Delta x^c = x_b + (i + 1/2) \Delta x \quad (14)$$

is the position of the center of cell i in coordinate direction $c \in \{1, 2, 3\}$. As an alternative, the grid spacing in any of the three grid directions can also be chosen to vary non-linearly. To achieve this, the user may supply up to three functions $f_c : [0, 1] \rightarrow [0, 1]$ satisfying $f(0) = 0$ and $f(1) = 1$, for which the only additional constraint is that its derivative $f'_c(\xi)$ be positive on $\xi \in [0, 1]$. Equation (14) is then replaced by

$$x_i^c = x_b^c + (x_e^c - x_b^c) f\left(\frac{i + 1/2}{N_c}\right). \quad (15)$$

Since this still satisfies $x_{-1/2} = x_b^c$ and $x_{N_c+1/2} = x_e^c$, the grid extent is left unchanged. Note that the identity mapping $f_{\text{lin}}(\xi) = \xi$ recovers the linear case. It is important that $f_c(\xi)$ be strictly monotonous also in the boundary cells beyond $\xi \in [0, 1]$, since these would otherwise get mapped into $[0, 1]$, i. e., the actual computational volume.

Several such non-linear grids are already pre-implemented in CRONOS; Table 1 provides a list of example mappings and their key properties. See also Section 8.4 for a test utilizing a non-linear grid.

3.2. Variables on the Grid

In CRONOS, the user works with the set of primitive variables, while the solver applies both, the primitive and the conserved variables. Ignoring the magnetic field for now, these

vectors are usually given as

$$\mathbf{U} = \begin{pmatrix} n \\ n\mathbf{u} \\ e \end{pmatrix} \quad \text{and} \quad \mathbf{U}_{\text{prim}} = \begin{pmatrix} n \\ \mathbf{u} \\ e_{\text{th}} \end{pmatrix}. \quad (16)$$

Instead of the thermal energy e_{th} , the temperature may alternatively be used as the primitive energy variable in CRONOS. This conveniently allows, e.g., a lower or upper limit for the temperature to be enforced within a simulation. By using the vector of conserved variables and by explicitly evaluating the conservation laws (10)–(13) for the different coordinate systems, they can be expressed as

$$\frac{\partial \mathbf{U}}{\partial t} + \frac{\partial \mathbf{F}}{\partial x} + \frac{\partial \mathbf{G}}{\partial y} + \frac{\partial \mathbf{H}}{\partial z} = \mathbf{s} \quad (17)$$

for Cartesian coordinates. Here, \mathbf{s} is again the vector of source terms, and \mathbf{F} , \mathbf{G} , \mathbf{H} are the physical fluxes in the three spatial dimensions. In cylindrical coordinates we find similarly

$$\frac{\partial \mathbf{U}}{\partial t} + \frac{1}{\rho} \frac{\partial}{\partial \rho} (\rho \mathbf{F}) + \frac{1}{\rho} \frac{\partial \mathbf{G}}{\partial \varphi} + \frac{\partial \mathbf{H}}{\partial z} = \mathbf{s} + \mathbf{s}_g, \quad (18)$$

and for spherical polar coordinates,

$$\begin{aligned} \frac{\partial \mathbf{U}}{\partial t} + \frac{1}{r^2} \frac{\partial}{\partial r} (r^2 \mathbf{F}) + \frac{1}{r \sin \vartheta} \frac{\partial}{\partial \vartheta} (\sin \vartheta \mathbf{G}) \\ + \frac{1}{r \sin \vartheta} \frac{\partial \mathbf{H}}{\partial \varphi} = \mathbf{s} + \mathbf{s}_g. \end{aligned} \quad (19)$$

Apart from the presence of the metric scale factors, there are also additional geometrical source terms \mathbf{s}_g that need to be taken into account in the non-Cartesian cases. These arise for the momentum equation only as a result of the divergence of the second-rank tensor $n\mathbf{u}\mathbf{u}$ (for details see, e.g., the appendix of Stone & Norman 1992a). Expressed in normalized form, the respective fluxes are

$$\mathbf{F} = \begin{pmatrix} nu_1 \\ nu_1^2 + p + B^2/2 - B_1^2 \\ nu_1 u_2 - B_1 B_2 \\ nu_1 u_3 - B_1 B_3 \\ (e + B^2/2 + p) u_1 - (\mathbf{B} \cdot \mathbf{u}) B_1 \end{pmatrix}, \quad (20)$$

$$\mathbf{G} = \begin{pmatrix} nu_2 \\ nu_1 u_2 - B_1 B_2 \\ nu_2^2 + p + B^2/2 - B_2^2 \\ nu_2 u_3 - B_2 B_3 \\ (e + B^2/2 + p) u_2 - (\mathbf{B} \cdot \mathbf{u}) B_2 \end{pmatrix}, \quad (21)$$

and

$$\mathbf{H} = \begin{pmatrix} nu_3 \\ nu_1 u_3 - B_1 B_3 \\ nu_2 u_3 - B_2 B_3 \\ nu_3^2 + p + B^2/2 - B_3^2 \\ (e + B^2/2 + p) u_3 - (\mathbf{B} \cdot \mathbf{u}) B_3 \end{pmatrix}. \quad (22)$$

In the discussion within this section, we have so far ignored the evolution of the magnetic field. For this, the induction equation can either be used as in Equation (12) or in the equiv-

Functional Form of $f_c(\xi)$	Ratio of Cell Sizes (left : center : right)	Comment
ξ	1 : 1 : 1	Standard linear case
$\frac{a^\xi - 1}{a - 1}$ ($a > 0, a \neq 1$)	1 : \sqrt{a} : a	Used in solar wind test
$\xi + \frac{a}{2\pi} \sin(2\pi \xi)$ ($ a < 1$)	$(1 + a) : (1 - a) : (1 + a)$	
$\begin{cases} (1 + a)\zeta & : \zeta \leq 1/2 \\ (1 - a)\zeta + a & : \zeta > 1/2 \end{cases}$ ($ a < 1$)	$(1 + a) : (\text{undef.}) : (1 - a)$	Used in Kleimann et al. (2017); transition can be shifted

Table 1

A list of several possible grid mappings to obtain increased resolution near selected grid planes, with important properties. The cell size at the normalized position ξ_0 is approximately proportional to $f'_c(\xi_0)$, and a is a free constant parameter.

alent conservative form:

$$\begin{aligned} \frac{\partial \mathbf{B}}{\partial t} &= \nabla \cdot \begin{pmatrix} 0 & E_3 & -E_2 \\ -E_3 & 0 & E_1 \\ E_2 & -E_1 & 0 \end{pmatrix} \\ &= \nabla \cdot \begin{pmatrix} 0 & -u_1 B_2 + u_2 B_1 & u_3 B_1 - u_1 B_3 \\ u_1 B_2 - u_2 B_1 & 0 & -u_2 B_3 + u_3 B_2 \\ -u_3 B_1 + u_1 B_3 & u_2 B_3 - u_3 B_2 & 0 \end{pmatrix} \end{aligned}$$

which can be rewritten as

$$\frac{\partial \mathbf{B}}{\partial t} + \nabla \cdot (\mathbf{u}\mathbf{B} - \mathbf{B}\mathbf{u}) = \mathbf{0}. \quad (23)$$

From this, one can compute the related fluxes as for the HD variables:

$$\begin{aligned} \mathbf{F}^B &= (u_1 \mathbf{B} - B_1 \mathbf{u}); & \mathbf{G}^B &= (u_2 \mathbf{B} - B_2 \mathbf{u}); \\ \mathbf{H}^B &= (u_3 \mathbf{B} - B_3 \mathbf{u}). \end{aligned} \quad (24)$$

The magnetic induction additionally has to fulfill the solenoidality condition

$$\nabla \cdot \mathbf{B} = 0. \quad (25)$$

Depending on whether Equation (12) or (23) is used to compute the time evolution of the magnetic induction, fulfilling the solenoidality condition is achieved by different methods in CRONOS, which will be discussed below. First, the finite-volume description of the code will be addressed.

4. SEMI-DISCRETE FINITE-VOLUME SCHEME

To numerically solve the system of Equations (10)–(13), the system of equations needs to be discretized. Two typical choices when using a grid code are discretization by either finite difference (see, e.g. Stone & Norman 1992a) or finite volume. This is equivalent to using variables at either grid points or grid cells, respectively. In CRONOS, the latter form of discretization is used, since a finite-volume code naturally fulfills conservation laws. Thus, handling of discontinuities, and in particular, shocks, is more natural than in a finite-difference code.

In a finite-volume scheme, the discretization results from integrating over the volume of a cell $C_{i,j,k}$. In CRONOS, the cell $C_{i,j,k}$ has the extent $[x_{i-\frac{1}{2}} \dots x_{i+\frac{1}{2}}] \times [y_{j-\frac{1}{2}} \dots y_{j+\frac{1}{2}}] \times$

$[z_{k-\frac{1}{2}} \dots z_{k+\frac{1}{2}}]$. By integrating Equation (17) over the volume of such a cell while using Gauss's theorem and dividing by the volume of the cell, one can find, for Cartesian coordinates,

$$\begin{aligned} \frac{\partial}{\partial t} \bar{\mathbf{U}}_{i,j,k} &+ \frac{\bar{\mathbf{F}}_{i+\frac{1}{2},j,k} - \bar{\mathbf{F}}_{i-\frac{1}{2},j,k}}{\Delta x} \\ &+ \frac{\bar{\mathbf{G}}_{i,j+\frac{1}{2},k} - \bar{\mathbf{G}}_{i,j-\frac{1}{2},k}}{\Delta y} \\ &+ \frac{\bar{\mathbf{H}}_{i,j,k+\frac{1}{2}} - \bar{\mathbf{H}}_{i,j,k-\frac{1}{2}}}{\Delta z} = \bar{\mathbf{s}}_{i,j,k}, \end{aligned} \quad (26)$$

with Δx , Δy , and Δz the extent of the cell in each of the three spatial dimensions. Here we introduced the cell average $\bar{\mathbf{w}}_{i,j,k}$ for a vector field given in cell (i, j, k) according to

$$\bar{\mathbf{w}}_{i,j,k} \equiv \frac{1}{\Delta x \Delta y \Delta z} \int_{x_{i-\frac{1}{2}}}^{x_{i+\frac{1}{2}}} \int_{y_{j-\frac{1}{2}}}^{y_{j+\frac{1}{2}}} \int_{z_{k-\frac{1}{2}}}^{z_{k+\frac{1}{2}}} \mathbf{w}(x, y, z) dx dy dz. \quad (27)$$

In contrast to this, the fluxes in Equation (26),

$$\bar{\mathbf{F}}_{i+\frac{1}{2},j,k} = \frac{1}{\Delta y \Delta z} \int_{y_{j-\frac{1}{2}}}^{y_{j+\frac{1}{2}}} \int_{z_{k-\frac{1}{2}}}^{z_{k+\frac{1}{2}}} \mathbf{F}(x_{i+\frac{1}{2}}, y, z) dy dz \quad (28)$$

$$\bar{\mathbf{G}}_{i,j+\frac{1}{2},k} = \frac{1}{\Delta x \Delta z} \int_{x_{i-\frac{1}{2}}}^{x_{i+\frac{1}{2}}} \int_{z_{k-\frac{1}{2}}}^{z_{k+\frac{1}{2}}} \mathbf{G}(x, y_{j+\frac{1}{2}}, z) dx dz \quad (29)$$

$$\bar{\mathbf{H}}_{i,j,k+\frac{1}{2}} = \frac{1}{\Delta x \Delta y} \int_{x_{i-\frac{1}{2}}}^{x_{i+\frac{1}{2}}} \int_{y_{j-\frac{1}{2}}}^{y_{j+\frac{1}{2}}} \mathbf{H}(x, y, z_{k+\frac{1}{2}}) dx dy \quad (30)$$

are averages over the cell's faces instead of over its volume. The resulting time-evolution Equation (26) is a so-called semi-discrete expression because the spatial derivatives have been discretized, while the temporal derivative has not. Thus, Equation (26) represents an ordinary differential equation (ODE) at each grid point. For completeness, we also show the general form of Equation (26) using arbitrary orthogonal coordinates:

$$\begin{aligned}
\frac{\partial \mathbf{U}}{\partial t} &+ \left(\frac{h_2(x_{i+\frac{1}{2}}, y_j, z_k) h_3(x_{i+\frac{1}{2}}, y_j, z_k) \bar{\mathbf{F}}_{i+\frac{1}{2},j,k} - h_2(x_{i-\frac{1}{2}}, y_j, z_k) h_3(x_{i-\frac{1}{2}}, y_j, z_k) \bar{\mathbf{F}}_{i-\frac{1}{2},j,k}}{h_1(x_i, y_j, z_k) h_2(x_i, y_j, z_k) h_3(x_i, y_j, z_k) \Delta x} \right) \\
&+ \left(\frac{h_1(x_i, y_{j+\frac{1}{2}}, z_k) h_3(x_i, y_{j+\frac{1}{2}}, z_k) \bar{\mathbf{G}}_{i,j+\frac{1}{2},k} - h_1(x_i, y_{j-\frac{1}{2}}, z_k) h_3(x_i, y_{j-\frac{1}{2}}, z_k) \bar{\mathbf{G}}_{i,j-\frac{1}{2},k}}{h_1(x_i, y_j, z_k) h_2(x_i, y_j, z_k) h_3(x_i, y_j, z_k) \Delta y} \right) \\
&+ \left(\frac{h_1(x_i, y_j, z_{k+\frac{1}{2}}) h_2(x_i, y_j, z_{k+\frac{1}{2}}) \bar{\mathbf{H}}_{i,j,k+\frac{1}{2}} - h_1(x_i, y_j, z_{k-\frac{1}{2}}) h_2(x_i, y_j, z_{k-\frac{1}{2}}) \bar{\mathbf{H}}_{i,j,k-\frac{1}{2}}}{h_1(x_i, y_j, z_k) h_2(x_i, y_j, z_k) h_3(x_i, y_j, z_k) \Delta z} \right) \\
&= \bar{\mathbf{s}}_{i,j,k}.
\end{aligned} \tag{31}$$

The following discussion will mostly consider the case of Cartesian coordinates.

In many numerical schemes, Equation (26) is further integrated over a discrete time interval Δt . This leads to a discrete grid in time, where the solution $\bar{\mathbf{w}}^{n+1}$ at time $t^n + \Delta t$ depends on the solution at the previous time step $\bar{\mathbf{w}}^n$ and the time integral of the fluxes through all cell boundaries:

$$\begin{aligned}
\bar{\mathbf{w}}_{i,j,k}^{n+1} &= \bar{\mathbf{w}}_{i,j,k}^n - \int_{t^n}^{t^{n+1}} \left(\frac{\bar{\mathbf{F}}_{i+\frac{1}{2},j,k} - \bar{\mathbf{F}}_{i-\frac{1}{2},j,k}}{\Delta x} \right. \\
&+ \frac{\bar{\mathbf{G}}_{i,j+\frac{1}{2},k} - \bar{\mathbf{G}}_{i,j-\frac{1}{2},k}}{\Delta y} \\
&+ \left. \frac{\bar{\mathbf{H}}_{i,j,k+\frac{1}{2}} - \bar{\mathbf{H}}_{i,j,k-\frac{1}{2}}}{\Delta z} + \bar{\mathbf{s}}_{i,j,k} \right) dt.
\end{aligned} \tag{32}$$

Unfortunately, this time integral cannot be solved analytically in general since it depends on \mathbf{w} for $t > t^n$ at the cell boundaries. Therefore, it is necessary to either find an analytical solution for the fluxes at the cell faces or to introduce a numerical approximation for these fluxes. Since analytical solutions are not available in all cases, and would in any case not even be significantly more accurate than an approximate solution, most codes employ numerical approximations to the fluxes at the cell faces. CRONOS allows for the use of various such Riemann solvers with different accuracy (see below).

In Godunov's method (Godunov 1959), the integrals were solved by assuming \mathbf{w} to be constant within a cell, leading to fluxes that are constant in time at the cell interfaces. This, however, led to a method first order in time and space. Such a first-order scheme is highly dissipative. Therefore, a higher-order approximation of the fluxes is used to find a more accurate approximation of the fluxes at the cell faces (Leveque 2002). Here, the use of a semi-discrete scheme allows a higher-order scheme to be implemented with relative ease, since using Equation (26) is equivalent to an independent discretization of space and time (Osher 1985; Kurganov & Tadmor 2000). CRONOS uses a second-order reconstruction in space together with an approximate Riemann solver that is evaluated at the present time step. In such a scheme, advancement in time can be done by any standard ODE solver. For CRONOS, we chose a second- or third-order TVD Runge-Kutta scheme (see, e.g., Shu 1988; Shu & Osher 1989).

5. TREATMENT OF THE MAGNETIC FIELD

In CRONOS, the magnetic field is handled differently from the other, hydrodynamic variables. This reflects the different evolution equation for the magnetic induction together with the solenoidality constraint (25). While the induction equation can be rewritten in the form Equation (23), only the original form of the induction equation, Equation (12), automatically implies that

$$\frac{\partial}{\partial t} (\nabla \cdot \mathbf{B}) = 0 \tag{33}$$

whereas Eq. (23) does not automatically conserve $\nabla \cdot \mathbf{B}$. Therefore, there are multiple methods available that can restore the constraint (25) even when using the conservative form of the induction equation. These methods include, e.g., divergence cleaning (see, e.g., Dedner et al. 2002) or the projection scheme. See Brackbill & Barnes (1980) for the first application of the projection scheme to MHD.

CRONOS instead applies the constrained transport method that is based on the original form of the induction equation. For a detailed description see, e.g., Evans & Hawley (1988) or Balsara & Spicer (1999). By computing the cell-averaged value of $\nabla \cdot \mathbf{B}$, the constraint (25) translates from a divergence to a difference equation of cell-area averages. For instance, in Cartesian coordinates one finds

$$\begin{aligned}
(\nabla \cdot \mathbf{B})_{i,j,k} &= \frac{1}{\Delta x \Delta y \Delta z} \int_{x_{i-\frac{1}{2}}}^{x_{i+\frac{1}{2}}} \int_{y_{j-\frac{1}{2}}}^{y_{j+\frac{1}{2}}} \int_{z_{k-\frac{1}{2}}}^{z_{k+\frac{1}{2}}} \nabla \cdot \mathbf{B}(x, y, z) dz dy dx \\
&= \frac{\bar{B}_1(x_{i+\frac{1}{2}}, y_j, z_k) - \bar{B}_1(x_{i-\frac{1}{2}}, y_j, z_k)}{\Delta x} \\
&+ \frac{\bar{B}_2(x_i, y_{j+\frac{1}{2}}, z_k) - \bar{B}_2(x_i, y_{j-\frac{1}{2}}, z_k)}{\Delta y} \\
&+ \frac{\bar{B}_3(x_i, y_j, z_{k+\frac{1}{2}}) - \bar{B}_3(x_i, y_j, z_{k-\frac{1}{2}})}{\Delta z},
\end{aligned} \tag{34}$$

where, as for the fluxes, the averages are taken over the cell

faces for the different magnetic field components:

$$\bar{B}_{1;i+\frac{1}{2},j,k} = \frac{1}{\Delta y \Delta z} \int_{y_j-\frac{1}{2}}^{y_j+\frac{1}{2}} \int_{z_{k-\frac{1}{2}}}^{z_{k+\frac{1}{2}}} B_1(x_{i+\frac{1}{2}}, y, z) dz dy \quad (35)$$

$$\bar{B}_{2;i,j+\frac{1}{2},k} = \frac{1}{\Delta x \Delta z} \int_{x_{i-\frac{1}{2}}}^{x_{i+\frac{1}{2}}} \int_{z_{k-\frac{1}{2}}}^{z_{k+\frac{1}{2}}} B_2(x, y_{j+\frac{1}{2}}, z) dz dx \quad (36)$$

$$\bar{B}_{3;i,j,k+\frac{1}{2}} = \frac{1}{\Delta x \Delta y} \int_{x_{i-\frac{1}{2}}}^{x_{i+\frac{1}{2}}} \int_{y_{j-\frac{1}{2}}}^{y_{j+\frac{1}{2}}} B_3(x, y, z_{k+\frac{1}{2}}) dy dx \quad (37)$$

This also shows that these area-averaged magnetic field components are the obvious choices for the magnetic field variables within a finite volume scheme (see also Gardiner & Stone 2005; Kissmann & Pomoell 2012). Each component is evolved by a quasi two-dimensional scheme within the corresponding cell face (Kissmann & Pomoell 2012). This scheme, however, also has to take into account the possibility that the dynamical variables may be subject to a jump in the direction normal to the cell face.

By computing the integral of Equation (12) over a cell face, one finds, in the form valid for all used coordinate systems,

$$\begin{aligned} \frac{\partial}{\partial t} \bar{B}_{1;i+\frac{1}{2},j,k} &= \frac{h_3(x_{i+\frac{1}{2}}, y_{j+\frac{1}{2}}, z_k) \bar{E}_{3;i+\frac{1}{2},j+\frac{1}{2},k} - h_3(x_{i+\frac{1}{2}}, y_{j-\frac{1}{2}}, z_k) \bar{E}_{3;i+\frac{1}{2},j-\frac{1}{2},k}}{h_2(x_{i+\frac{1}{2}}, y_j, z_k) h_3(x_{i+\frac{1}{2}}, y_j, z_k) \Delta y} \\ &\quad - \frac{h_2(x_{i+\frac{1}{2}}, y_j, z_{k+\frac{1}{2}}) \bar{E}_{2;i+\frac{1}{2},j,k+\frac{1}{2}} - h_2(x_{i+\frac{1}{2}}, y_j, z_{k-\frac{1}{2}}) \bar{E}_{2;i+\frac{1}{2},j,k-\frac{1}{2}}}{h_2(x_{i+\frac{1}{2}}, y_j, z_k) h_3(x_{i+\frac{1}{2}}, y_j, z_k) \Delta z} \end{aligned} \quad (38)$$

$$\begin{aligned} \frac{\partial}{\partial t} \bar{B}_{2;i,j+\frac{1}{2},k} &= \frac{h_1(x_i, y_{j+\frac{1}{2}}, z_{k+\frac{1}{2}}) \bar{E}_{1;i,j+\frac{1}{2},k+\frac{1}{2}} - h_1(x_i, y_{j+\frac{1}{2}}, z_{k-\frac{1}{2}}) \bar{E}_{1;i,j+\frac{1}{2},k-\frac{1}{2}}}{h_1(x_i, y_{j+\frac{1}{2}}, z_k) h_3(x_i, y_{j+\frac{1}{2}}, z_k) \Delta z} \\ &\quad - \frac{h_3(x_{i+\frac{1}{2}}, y_{j+\frac{1}{2}}, z_k) \bar{E}_{3;i+\frac{1}{2},j+\frac{1}{2},k} - h_3(x_{i-\frac{1}{2}}, y_{j+\frac{1}{2}}, z_k) \bar{E}_{3;i-\frac{1}{2},j+\frac{1}{2},k}}{h_1(x_i, y_{j+\frac{1}{2}}, z_k) h_3(x_i, y_{j+\frac{1}{2}}, z_k) \Delta x} \end{aligned} \quad (39)$$

$$\begin{aligned} \frac{\partial}{\partial t} \bar{B}_{3;i,j,k+\frac{1}{2}} &= \frac{h_2(x_{i+\frac{1}{2}}, y_j, z_{k+\frac{1}{2}}) \bar{E}_{2;i+\frac{1}{2},j,k+\frac{1}{2}} - h_2(x_{i-\frac{1}{2}}, y_j, z_{k+\frac{1}{2}}) \bar{E}_{2;i-\frac{1}{2},j,k+\frac{1}{2}}}{h_1(x_i, y_j, z_{k+\frac{1}{2}}) h_2(x_i, y_j, z_{k+\frac{1}{2}}) \Delta x} \\ &\quad - \frac{h_1(x_{i+\frac{1}{2}}, y_{j+\frac{1}{2}}, z_k) \bar{E}_{1;i+\frac{1}{2},j+\frac{1}{2},k} - h_1(x_{i+\frac{1}{2}}, y_{j-\frac{1}{2}}, z_k) \bar{E}_{1;i+\frac{1}{2},j-\frac{1}{2},k}}{h_1(x_i, y_j, z_{k+\frac{1}{2}}) h_2(x_i, y_j, z_{k+\frac{1}{2}}) \Delta y} \end{aligned} \quad (40)$$

where the \bar{E}_i are line-averaged components of the electric field $\mathbf{E} = -\mathbf{v} \times \mathbf{B}$. These line averages are given by

$$\bar{E}_{1;i,j+\frac{1}{2},k+\frac{1}{2}} = \frac{1}{\Delta x} \int_{x_{i-\frac{1}{2}}}^{x_{i+\frac{1}{2}}} E_1(x, y_{j+\frac{1}{2}}, z_{k+\frac{1}{2}}) dx, \quad (41)$$

$$\bar{E}_{2;i+\frac{1}{2},j,k+\frac{1}{2}} = \frac{1}{\Delta y} \int_{y_{j-\frac{1}{2}}}^{y_{j+\frac{1}{2}}} E_1(x_{i+\frac{1}{2}}, y, z_{k+\frac{1}{2}}) dy, \quad (42)$$

$$\bar{E}_{3;i+\frac{1}{2},j+\frac{1}{2},k} = \frac{1}{\Delta z} \int_{z_{k-\frac{1}{2}}}^{z_{k+\frac{1}{2}}} E_3(x_{i+\frac{1}{2}}, y_{k+\frac{1}{2}}, z) dz. \quad (43)$$

For hydrodynamics the dynamical variables are given at the cell centers, with their fluxes given at the cell faces. In contrast to that, the vector components of the magnetic induction are given on the respective cell faces, with the related electric fields given at the cell edges. For an illustration, see Figure 1, or Balsara & Spicer (1999) and Ziegler (2004).

The different collocation points of the magnetic field and the HD variables also mean that a cell-centered absolute magnetic field needs to be computed for the transition from primitive to conservative variables (see Equation (16)). In agreement with the second-order nature of the code this is done via linear interpolation:

$$B_{i,j,k}^2 = \left(\frac{\bar{B}_{1;i+\frac{1}{2},j,k} + \bar{B}_{1;i-\frac{1}{2},j,k}}{2} \right)^2 + \left(\frac{\bar{B}_{2;i,j+\frac{1}{2},k} + \bar{B}_{2;i,j-\frac{1}{2},k}}{2} \right)^2 + \left(\frac{\bar{B}_{3;i,j,k+\frac{1}{2}} + \bar{B}_{3;i,j,k-\frac{1}{2}}}{2} \right)^2 \quad (44)$$

No slope limiter (see below) is necessary for this averaging since the magnetic field components are continuous along the direction of averaging due to constraint (25). In the next step, we will discuss the numerical integration of the dynamical variables.

6. THE NUMERICAL SCHEME

The description of the numerical scheme is starts with a one-dimensional (1D) analogy, whereas the code itself is 3D. While this 1D description does not directly reflect the actual implementation within the code, it is useful to illustrate the basic ideas behind the numerical implementation. Subsequently, the 3D MHD scheme of CRONOS is introduced, where the extension from 1D to 3D is helped by the semi-discrete nature of the scheme. Numerical integration of the magnetic induction is only discussed in the context of the 3D scheme.

6.1. The One-dimensional Scheme

In the discussion of the 1D scheme it is assumed that only equations of the form

$$\frac{\partial \mathbf{U}}{\partial t} + \frac{\partial \mathbf{F}}{\partial x} = \mathbf{s} \quad (45)$$

are taken into account. Here, only Cartesian coordinates will be addressed since an extension to arbitrary coordinates can be found with relative ease. Additionally, only HD plus possible tracer fields are taken into account, while the MHD case will be discussed in the context of the 3D scheme. Thus, the vector of physical fluxes is

$$\mathbf{F} = \begin{pmatrix} nu_x \\ nu_x^2 + p \\ nu_x u_y \\ nu_x u_z \\ (e + p) u_x \end{pmatrix}, \quad (46)$$

with the corresponding vector of primitive or conserved variables given in Equation (16). Additionally, the flux vector

can be extended by the flux for a tracer field $F_t = \Phi nu_x$ with the corresponding conserved variable $h = \Phi n$. In the semi-discrete framework, the finite-volume discretization of Equation (45) is

$$\frac{\partial \bar{\mathbf{U}}_i}{\partial t} + \frac{\bar{\mathbf{F}}_{i+\frac{1}{2}} - \bar{\mathbf{F}}_{i-\frac{1}{2}}}{\Delta x} = \bar{\mathbf{s}} \quad (47)$$

according to Equation (26), with

$$\bar{\mathbf{U}} = \frac{1}{\Delta x} \int_{i-\frac{1}{2}}^{i+\frac{1}{2}} \mathbf{U}(x, t) dx \quad (48)$$

and $\bar{\mathbf{F}}_{i\pm\frac{1}{2}}$ the fluxes on the cell faces. In a semi-discrete scheme as that used in CRONOS, time-integration is done using an arbitrary ODE solver. While Equation (47) is still exact, a numerical approximation is used in computing the fluxes $\bar{\mathbf{F}}_{i\pm\frac{1}{2}}$. This approximation usually is twofold: first, the dynamical variables are given as volume averages. Thus, some interpolation procedure is necessary in order to compute the local fluxes at the position of the cell interfaces. Second, since the reconstructed flux values at the cell interface are not unique, a numerical estimate is used to compute a corresponding unique flux. On top of that, a numerical quadrature rule is used to solve the system of ODEs (47).

The interpolation procedure, usually referred to as spatial reconstruction, is used to compute point values from the cell averages of the dynamical variables at the location of the cell interfaces. In a second-order code like CRONOS, reconstruction is done using a piecewise linear polynomial, i.e., a linear polynomial is found in each cell that can best approximate the solution within the local and the neighboring cells. Correspondingly, the point values at the cell interfaces are usually not unique, but differ for the reconstruction polynomials within the adjacent left- and the right-handed cells (see also LeVeque 2002, for further discussion).

The left- and right-handed states at each cell interface define a configuration similar to a Riemann problem, i.e., an initial value problem for a set of conservation equations together with piecewise constant data containing a jump. In the scheme by Godunov (1959) the system of PDEs was solved by assuming the data to be constant within each cell. Thus, the left- and right-handed states were spatially constant, and the time evolution of the dynamical variables at the cell interface could be computed by exploiting the fact that the solution of the Riemann problem is constant in time at the position of the interface. Even in this first-order case, the computation of an exact solution of the Riemann problem, however, is numerically rather expensive. Therefore, approximate Riemann solvers are usually applied.

Such a first-order method is usually not desirable since it leads to poor resolution in smooth regions of the flow. Therefore, different methods are in use to extend the scheme by Godunov (1959) to higher order (see, e.g., Toro 1997), where sophisticated methods are used to allow an application of a Riemann solver at the cell interfaces even when the reconstruction polynomials within the cells are of higher order. All such schemes need to address the problem that the state at the cell interface is not constant in time for non-constant states within the cells. A semi-discrete scheme, such as that used in CRONOS, is based on the assumption that $\Delta t \rightarrow 0$. Therefore, the Riemann problem at the cell interface is only

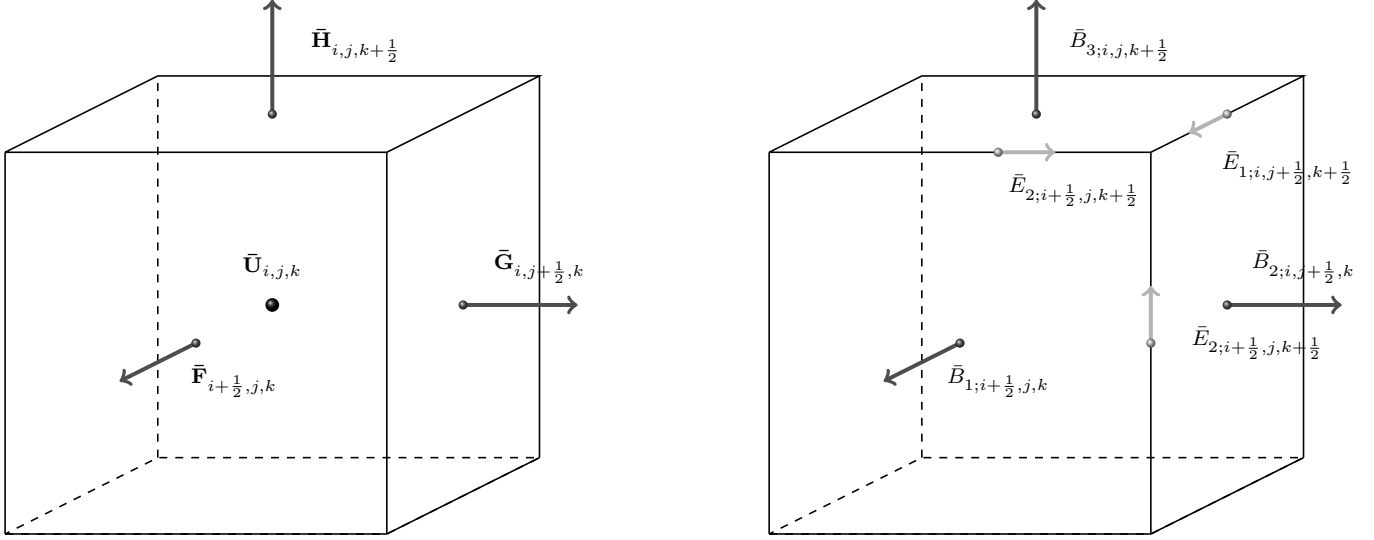


Figure 1. Illustration of cell $C_{i,j,k}$ in Cartesian coordinates. The collocation points of the hydrodynamic (left) and the magnetic field (right) variables are shown together with the corresponding fluxes and electric fields.

evaluated at time t^n without the need to compute the time evolution of the flux on the cell interface. Thus, it is also possible to apply a given Riemann solver in the same form as in the Godunov scheme even for a higher-order interpolation of the fluxes. Using $\Delta t \rightarrow 0$ means that the solution of the Riemann problem only requires the left- and right-handed values at the cell interface.

6.2. Specifics of the One-dimensional Scheme

Next, the implementation is discussed in the context of a one-dimensional setup. Due to the semi-discrete nature of the scheme, the time integration and the solution of the Riemann problem can be discussed independently. To compute the time integral, we use a second- or third-order-accurate Runge–Kutta scheme. This means that a Riemann problem needs to be solved at each of the two or three substeps.

The solution at each substep can then again be split into several steps: reconstruction of point values at cell interfaces, computation of characteristic velocities, computation of numerical flux approximations at cell interfaces, update of cell-centered variables using numerical fluxes, and advancement to the next substep of the time-integration scheme. This procedure is also illustrated in Figure 2. In the following, we will address each of those steps individually.

6.2.1. Reconstruction

In the reconstruction procedure, the point values at the left- and right-handed cell interfaces are computed for each cell from the cell averages. CRONOS uses a piecewise-linear reconstruction polynomial for each primitive variable q , i.e., in cell C_i , the point values at the left- and right-handed cell interface are given as

$$q_i^{\text{L,R}} = \bar{q}_i \pm \frac{1}{2} (\delta \bar{q})_i, \quad (49)$$

where $(\delta \bar{q})_i$ is an estimate for the linear slope in cell C_i . Here, “L” and “R” refer to the point values at the left- and right-handed interface of cell C_i . To avoid spurious oscillations near discontinuities in the flow, a slope limiter is applied. For

this, CRONOS computes three different estimates for the linear slope using the data in the adjacent cells:

$$\delta_{\text{L},i} = \frac{\bar{q}_i - \bar{q}_{i-1}}{x_i - x_{i-1}}; \quad \delta_{\text{C},i} = \frac{\bar{q}_{i+1} - \bar{q}_{i-1}}{x_{i+1} - x_{i-1}}; \quad \delta_{\text{R},i} = \frac{\bar{q}_{i+1} - \bar{q}_i}{x_{i+1} - x_i}. \quad (50)$$

From these, a non-oscillatory slope is computed by using a slope limiter L as

$$(\delta \bar{q})_i = L(\delta_{\text{L},i}, \delta_{\text{C},i}, \delta_{\text{R},i}). \quad (51)$$

Currently, the van Leer limiter (see van Leer 1977)

$$(\delta \bar{q})_i = \frac{\max(\delta_{\text{R},i}, \delta_{\text{L},i}, 0)}{\delta_{\text{C},i}}, \quad (52)$$

the family of minmod limiters (see van Leer 1979; Harten 1983)

$$(\delta \bar{q})_i = \text{minmod}(\Theta \delta_{\text{L},i}, \delta_{\text{C},i}, \Theta \delta_{\text{R},i}), \quad (53)$$

where for the latter $\Theta \in [1, 2]$ and

$$\text{minmod}(a, b, c) = \begin{cases} \min(a, b, c) & \text{if } a, b, c > 0 \\ \max(a, b, c) & \text{if } a, b, c < 0 \\ 0 & \text{else} \end{cases}, \quad (54)$$

and additionally the superbee limiter (Roe 1985)

$$(\delta \bar{q})_i = \text{maxmod}(\delta_i^{(1)}, \delta_i^{(2)}) \quad (55)$$

with

$$\delta_i^{(1)} = \text{minmod}(\delta_{\text{R},i}, 2\delta_{\text{L},i}) \quad (56)$$

$$\delta_i^{(2)} = \text{minmod}(2\delta_{\text{R},i}, \delta_{\text{L},i}) \quad (57)$$

are supported. In the latter case, the maxmod function is defined in analogy to the minmod function but using the maximum instead of the minimum.

The setup of the limiter can be chosen via the parameter file. Due to the realization via inheritance from a corresponding base class, inclusion of additional limiters into CRONOS can be achieved with relative ease.

The point values at the cell interfaces are computed locally for each cell. Thus, at the cell interface at $i + \frac{1}{2}$, we find

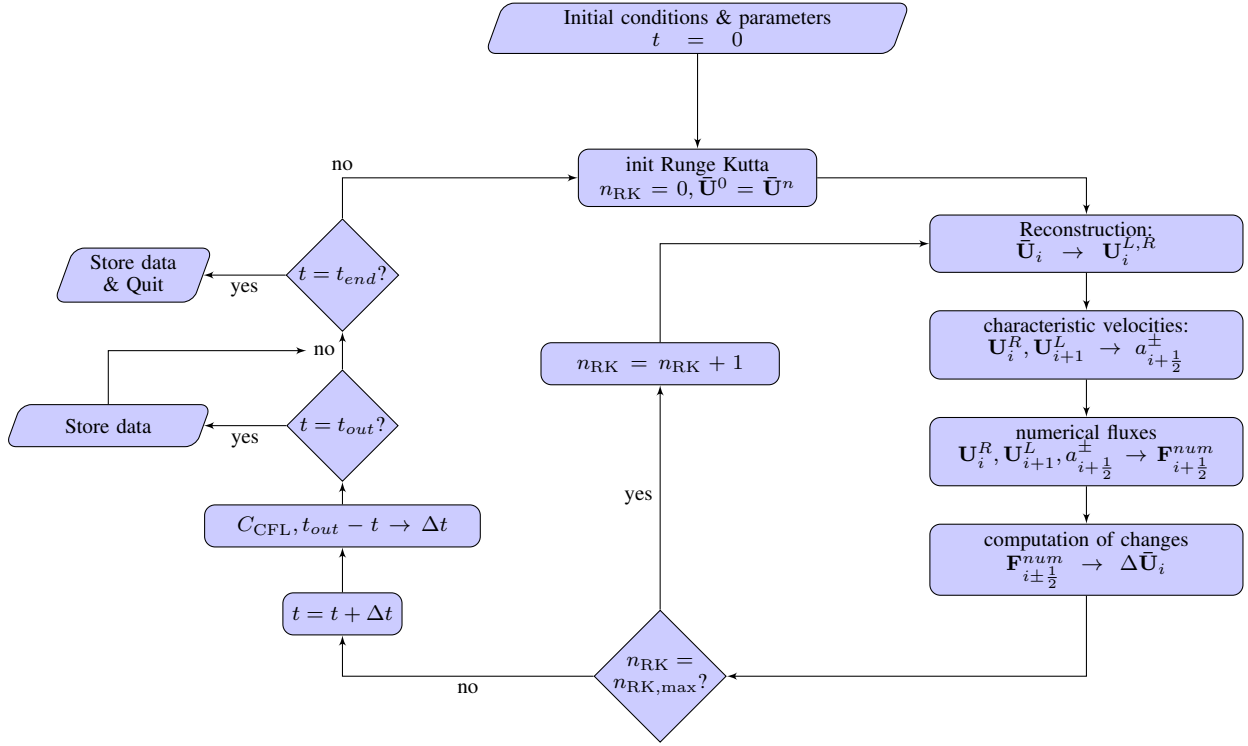


Figure 2. Flowchart for the 1D scheme used in the CRONOS code. Here, n denotes the substep of the Runge–Kutta time-integration scheme.

the two different point values q_i^R and q_{i+1}^L , which refer to the point values computed in the cells on the left and the right side of the cell interface, respectively. Additionally, these point values are used to compute the corresponding flux values \mathbf{F}_i^R and \mathbf{F}_{i+1}^L as given in Equation (46). The point values are then used to compute the characteristic velocities and the numerical fluxes in the next steps.

6.2.2. Characteristic Velocities

All approximate Riemann solvers used within the CRONOS code need an estimate of the maximum (a^+) and minimum (a^-) characteristic velocities at the cell interfaces. In general, these are given by the eigenvalues of the Jacobian of the system of PDEs:

$$a_{i+\frac{1}{2}}^+ := \max_{q \in \{q_i^R, q_{i+1}^L\}} \left\{ \lambda_N \left(\frac{\partial \mathbf{F}}{\partial \mathbf{U}}(q) \right), 0 \right\}; \quad (58)$$

$$a_{i+\frac{1}{2}}^- := - \min_{q \in \{q_i^R, q_{i+1}^L\}} \left\{ \lambda_1 \left(\frac{\partial \mathbf{F}}{\partial \mathbf{U}}(q) \right), 0 \right\}.$$

For the implementation of the HD solver in CRONOS, these are computed from the local point values according to

$$a_{i+\frac{1}{2}}^+ = \max \left\{ (c_s + u_x)_{i,j,k}^R, (c_s + u_x)_{i+1,j,k}^L, 0 \right\}, \quad (59)$$

$$a_{i+\frac{1}{2}}^- = \max \left\{ (c_s - u_x)_{i,j,k}^R, (c_s - u_x)_{i+1,j,k}^L, 0 \right\}, \quad (60)$$

where $c_s = (\gamma p/n)^{1/2}$ is the speed of sound in normalized units. Accordingly, the characteristic velocities are defined as being directed to the right for $a_{i+\frac{1}{2}}^+$ and to the left for $a_{i+\frac{1}{2}}^-$, leading to $a_{i+\frac{1}{2}}^{\pm} \geq 0$.

6.2.3. Computation of Numerical Fluxes

In the third step, the numerical fluxes are computed from the left- and right-handed values of the dynamical variables and the physical fluxes given at the cell interfaces using the estimates for the characteristic velocities. In CRONOS, only approximate Riemann solvers are used, where currently HLL, HLLC, and HLLD are supported, with the latter exclusively applicable to the MHD case. Of these, the HLL originally proposed by Harten et al. (1983) is the simplest Riemann solver, where the numerical flux is computed as

$$\mathbf{F}_{i+\frac{1}{2}}^{\text{HLL}} = \frac{a_{i+\frac{1}{2}}^- \mathbf{F}_{i+1}^L + a_{i+\frac{1}{2}}^+ \mathbf{F}_i^R - a_{i+\frac{1}{2}}^- a_{i+\frac{1}{2}}^+ (\mathbf{U}_{i+1}^L - \mathbf{U}_i^R)}{a_{i+\frac{1}{2}}^+ + a_{i+\frac{1}{2}}^-}. \quad (61)$$

Together with the semi-discrete time-integration, this solver leads to the same numerical scheme as was introduced by Kurganov et al. (2001) and Ziegler (2004). Since the HLL solver does not require a characteristic decomposition, it is numerically much cheaper than, e.g., the one by Roe (Roe 1981) that solves the linearized Riemann problem. At the same time, the HLL solver approximates the Riemann problem by only a single, constant state between the fastest and the slowest wave mode. Therefore, contact discontinuities are reproduced only rather poorly.

To avoid this problem, Harten (1983) suggested restoring the missing wave in the approximate representation of the Riemann fan. This will improve the accuracy of the numerical approximation while making the approximate flux more problem-dependent: the numerical flux of the HLL Riemann solver only depends on the underlying system of PDEs via the estimates of the characteristic velocities a^+ and a^- . The missing intermediate states in the Riemann fan, however, are different for different systems of PDEs. In CRONOS, such an adapted solver for the HD case, the HLLC solver, is used as is

discussed in Toro et al. (1994) and Toro (1997). This solver was found to be very accurate while having a significantly lower computational cost than Roe's solver (see, e.g., Stone et al. 2008). Therefore, it is the solver recommended for most HD simulations with CRONOS.

6.2.4. Updates of Dynamical Variables and Time Integration

After the numerical fluxes through all faces of a cell are computed, the dynamical variables represented by the cell averages are updated according to Equation (47). Using the example of the second-order Runge–Kutta solver, this results in the scheme

$$\begin{aligned}\bar{\mathbf{U}}_i^* &= \bar{\mathbf{U}}_i^n + \left(\bar{\mathbf{s}}_i^n - \frac{\mathbf{F}_{i+\frac{1}{2}}^n - \mathbf{F}_{i-\frac{1}{2}}^n}{\Delta x} \right) \Delta t \\ \bar{\mathbf{U}}_i^{n+1} &= \frac{1}{2} (\bar{\mathbf{U}}_i^n + \bar{\mathbf{U}}_i^*) + \frac{1}{2} \left(\bar{\mathbf{s}}_i^* - \frac{\mathbf{F}_{i+\frac{1}{2}}^* - \mathbf{F}_{i-\frac{1}{2}}^*}{\Delta x} \right) \Delta t,\end{aligned}\quad (62)$$

where indices n , $n+1$, and \star signify the current, the next, and the intermediate time steps used in the Runge–Kutta time-integration scheme. This shows that the ease of using a semi-discrete scheme comes at the price of the Riemann solver having to be applied twice per time step: once at time t^n and once more at the intermediate time t^* . When using the third-order Runge–Kutta scheme, three Riemann problems need to be solved at each cell interface to advance a single time step. After completing all sub-steps of the respective Runge–Kutta scheme, the solution procedure starts again at the next time step t^{n+1} .

After finishing the full Runge–Kutta scheme for time step t^n , a new size of the full time step $\Delta t = t^{n+1} - t^n$ is computed dynamically using the Courant–Friedrichs–Lewy (CFL) condition (see Courant et al. 1928)

$$C_{\text{CFL}} \geq \max_i \left(\frac{a_{i-\frac{1}{2}}^{\max} \Delta t}{\Delta x} \right), \quad (63)$$

where $a_{i-\frac{1}{2}}^{\max}$ signifies the largest characteristic speed computed at cell face $i - \frac{1}{2}$. Here, we simply reuse the characteristic speeds computed for the numerical fluxes.

In case of the scheme used in CRONOS, constraint (63) has to make sure that the characteristics from any face of the cell cannot interact with those of the other cell face. This is reflected by $C_{\text{CFL}} \geq 0.5$. In CRONOS typically a limit of $C_{\text{CFL}} = 0.4$ is used, which is also compatible with the limit for the Runge–Kutta time integrator of 0.42 found by Pareschi et al. (2005). Since this value is given in CRONOS's parameter file, it can be easily adapted by the user.

To allow an output at regular time intervals chosen by the user, sometimes time steps that are smaller than required by conditions (63) are used. Like with the intermediate output, CRONOS also checks whether the desired end time t_{end} of the simulation has been reached and stops accordingly.

6.3. The Three-dimensional Solver

Having introduced the 1D solver, the 3D scheme is discussed in the following. Here, the focus will be on the differences as compared to the 1D scheme. These, particularly, include the time evolution of the magnetic induction that is best discussed in the multidimensional

case. Before we come to that, we discuss the extension of the 1D scheme for hydrodynamics to three spatial dimensions.

6.3.1. The Hydrodynamics Scheme

The scheme for the system of HD equations is very similar to the 1D case. In this case, the reconstruction yields left- and right-handed point values for all cell faces: q_i^{W} , q_i^{E} , q_i^{S} , q_i^{N} , q_i^{B} , q_i^{T} , where the superscripts are related to the positions at the centers of the cell faces, $\text{W} \leftrightarrow (x_{i-\frac{1}{2}}, y_j, z_k)$, $\text{E} \leftrightarrow (x_{i+\frac{1}{2}}, y_j, z_k)$, $\text{S} \leftrightarrow (x_i, y_{j-\frac{1}{2}}, z_k)$, $\text{N} \leftrightarrow (x_i, y_{j+\frac{1}{2}}, z_k)$, $\text{B} \leftrightarrow (x_i, y_j, z_{k-\frac{1}{2}})$, and $\text{T} \leftrightarrow (x_i, y_j, z_{k+\frac{1}{2}})$. The slopes for this reconstruction are computed only along the relevant direction, e.g., we have for the y -direction

$$\begin{aligned}q_{i,j,k}^{\text{S,N}} &= \bar{q}_{i,j,k} \pm \frac{1}{2} (\delta \bar{q})_{i,j,k} \\ \text{with } (\delta \bar{q})_{i,j,k} &= L \left(\delta_{L;i,j,k}^y, \delta_{C;i,j,k}^y, \delta_{R;i,j,k}^y \right),\end{aligned}\quad (64)$$

where the same limiters L as in the 1D case are used. Additionally, the relevant slopes are

$$\begin{aligned}\delta_{L;i,j,k}^y &= \frac{\bar{q}_{i,j,k} - \bar{q}_{i,j-1,k}}{y_j - y_{j-1}}; & \delta_{C;i,j,k}^y &= \frac{\bar{q}_{i,j+1,k} - \bar{q}_{i,j-1,k}}{y_{j+1} - y_{j-1}}; \\ \delta_{R;i,j,k}^y &= \frac{\bar{q}_{i,j+1,k} - \bar{q}_{i,j,k}}{y_{j+1} - y_j}\end{aligned}\quad (65)$$

for the y -dimension, with respective expressions for the other spatial dimensions.

From these point values, characteristic velocities are computed for all cell faces, resulting in $a_{i+\frac{1}{2},j,k}^{\pm}$, $b_{i,j+\frac{1}{2},k}^{\pm}$, and $c_{i,j,k+\frac{1}{2}}^{\pm}$ at the upper x , y , and z faces, respectively. In the most general form, these are given as

$$a_{i+\frac{1}{2},j,k}^+ := \max_{q \in \{q_{i,j,k}^{\text{E}}, q_{i+1,j,k}^{\text{W}}\}} \left\{ \lambda_{\text{N}} \left(\frac{\partial \mathbf{F}}{\partial \mathbf{U}}(q) \right), 0 \right\}; \quad (66)$$

$$a_{i+\frac{1}{2},j,k}^- := \min_{q \in \{q_{i,j,k}^{\text{E}}, q_{i+1,j,k}^{\text{W}}\}} \left\{ \lambda_1 \left(\frac{\partial \mathbf{F}}{\partial \mathbf{U}}(q) \right), 0 \right\}; \quad (67)$$

$$b_{i,j+\frac{1}{2},k}^+ := \max_{q \in \{q_{i,j,k}^{\text{N}}, q_{i,j+1,k}^{\text{S}}\}} \left\{ \lambda_{\text{N}} \left(\frac{\partial \mathbf{G}}{\partial \mathbf{U}}(q) \right), 0 \right\}; \quad (68)$$

$$b_{i,j+\frac{1}{2},k}^- := \min_{q \in \{q_{i,j,k}^{\text{N}}, q_{i,j+1,k}^{\text{S}}\}} \left\{ \lambda_1 \left(\frac{\partial \mathbf{G}}{\partial \mathbf{U}}(q) \right), 0 \right\}; \quad (69)$$

$$c_{i,j,k+\frac{1}{2}}^+ := \max_{q \in \{q_{i,j,k}^{\text{T}}, q_{i,j,k+1}^{\text{B}}\}} \left\{ \lambda_{\text{N}} \left(\frac{\partial \mathbf{H}}{\partial \mathbf{U}}(q) \right), 0 \right\}; \quad (70)$$

$$c_{i,j,k+\frac{1}{2}}^- := \min_{q \in \{q_{i,j,k}^{\text{T}}, q_{i,j,k+1}^{\text{B}}\}} \left\{ \lambda_1 \left(\frac{\partial \mathbf{H}}{\partial \mathbf{U}}(q) \right), 0 \right\}. \quad (71)$$

In CRONOS, this is approximated using Equations (59) and (60), where instead of u_x the velocity component along the normal of the respective cell face is used.

Using the characteristic velocities, the numerical fluxes are computed at each cell face from the respective left- and right-handed point values. For this, the same Riemann solvers as in the 1D scheme can be applied, because the numerical fluxes are only needed at the centers of each cell face where the Riemann problem is determined by the jump of the variables between the cells separated by the cell face. Using the Riemann

problem at the center of the cell face only leads to a second-order approximation of the integrals of the fluxes over the respective cell faces (see Equations (28)–(30)), consistent with the second-order reconstruction. As in the 1D solver, use of the HLLC Riemann solver is recommended for HD problems. Time integration is done in the same way as in the 1D scheme, where the CFL conditions is

$$C_{\text{CFL}} \geq \max_{i,j,k} \left(\max \left(\frac{a_{i-\frac{1}{2},j,k}^{\max} \Delta t}{\Delta x}, \frac{b_{i,j-\frac{1}{2},k}^{\max} \Delta t}{\Delta y}, \frac{c_{i,j,k-\frac{1}{2}}^{\max} \Delta t}{\Delta z} \right) \right). \quad (72)$$

6.3.2. The Scheme for MHD

The presence of the induction equation necessitates some changes for the numerical scheme for the treatment of this equation. As was discussed in Section 5, the components of the magnetic field are evolved as cell-face averages according to Equations (35)–(40). As with the fluxes in the HD scheme, a numerical approximation for the electric field at the cell edges now needs to be computed (see Figure 1). This suffers from the additional complication that the reconstructed variables can be discontinuous in both directions perpendicular to the respective cell edges. Thus, the evolution of each component of the magnetic induction is subject to a 2D Riemann problem at the collocation points of the respective electric fields.

Despite this problem, the use of cell-face centered magnetic-field components allows for a natural implementation of the solenoidality constraint, with this collocation for the magnetic field components directly following for a finite-volume scheme as shown in Section 5. While there is no analytical solution for these 2D Riemann problems, there are multiple approaches for an implementation of the constrained transport scheme using cell-face-centered components of the magnetic induction (see, e.g., Balsara & Spicer 1999; Tóth 2000; Ziegler 2004; Gardiner & Stone 2005, 2008; Londrillo & Del Zanna 2000, 2004).

These approaches can be separated into two fundamental groups. In the first, the solution to the 1D Riemann problems at the centers of the cell faces is interpolated to the cell edges to give an approximation to the 2D Riemann problem there. In the second approach, the 1D approximate Riemann solver is extended to two spatial dimensions. The resulting 2D approximate Riemann solver then is evaluated directly at the respective cell edges.

6.3.3. Constrained Transport using Face-centered Fluxes

The first approach is based on the induction equation given in the form of Equation (23). While this equation relates to the use of cell-centered variables, it is only used to compute numerical flux estimates for the magnetic induction at the cell faces. According to Equation (23) the related physical fluxes are

$$\mathbf{F}^B = \begin{pmatrix} 0 \\ -E_3 \\ E_2 \end{pmatrix}; \quad \mathbf{G}^B = \begin{pmatrix} E_3 \\ 0 \\ -E_1 \end{pmatrix}; \quad \mathbf{H}^B = \begin{pmatrix} -E_2 \\ E_1 \\ 0 \end{pmatrix}, \quad (73)$$

which signify the respective fluxes in the x -, y -, and z -directions. Like the HD fluxes, they are also defined at the

centers of the respective cell faces. Thus, the same approximate Riemann solvers are used to compute numerical fluxes. In addition to the HLL and HLLC solvers discussed above, CRONOS also features the HLLD solver for MHD problems.

In the development of the HLLD Riemann solver, a similar strategy to that for the HLLC solver was employed. Instead of using two intermediate states in the Riemann solver, Miyoshi & Kusano (2005) derived the HLLD solver for MHD using four intermediate states. Apart from the contact discontinuity recovered by the HLLC solver, they also included two Alfvén waves within the Riemann fan. Like the HLLC solver for HD problems, the HLLD solver is very efficient for MHD problems. In CRONOS, both this form of the HLLD solver and the one suggested by Mignone (2007) for isothermal problems are used.

Using a Riemann solver for the combined fluxes (73) and (20)–(22) leads to a numerical estimate for these fluxes at the centers of each cell face. The simplest approach to obtain a numerical estimate for the electric fields at the cell edges is a direct averaging of the related fluxes on the faces adjacent to the respective cell edges as discussed in Balsara & Spicer (1999) and Ziegler (2004). This leads, e.g., to

$$E_{1,i,j+\frac{1}{2},k+\frac{1}{2}}^{\text{HLLX}} = \frac{1}{4} \left(H_{2;i,j,k+\frac{1}{2}}^{B,\text{HLLX}} + H_{2;i,j+1,k+\frac{1}{2}}^{B,\text{HLLX}} - G_{3;i,j+\frac{1}{2},k}^{B,\text{HLLX}} - G_{3;i,j+\frac{1}{2},k+1}^{B,\text{HLLX}} \right) \quad (74)$$

and similar expressions for the other components (see also Equations (7)–(9) in Balsara & Spicer 1999), where HLLX indicates that the fluxes were computed using one of the approximate Riemann solvers.

Gardiner & Stone (2005, 2008), however, showed that this averaging of fluxes that are not given locally at the cell edges can lead to problems, since this scheme is inconsistent with plane-parallel grid-aligned flow in one dimension and can lead to spurious oscillations in multidimensional configurations. Accordingly, they suggest more complex averaging procedures that use a projection of the fluxes to the positions of the cell edges. In CRONOS, we allow for the use of the corresponding expressions provided by Gardiner & Stone (2005, 2008) for the computation of the numerical electric fields.

6.3.4. Constrained Transport using Cell-edge Related Electric Fields

In the second approach available in CRONOS, the numerical estimate for the electric fields is directly computed at the cell edges. This is done by a direct extension of the 1D Riemann solver to a 2D Riemann problem. Currently, this is only implemented for the HLL Riemann solver in CRONOS.

An extension of the HLL solver is, again, done by assuming a single constant state within the 2D Riemann fan. This Riemann fan is assumed to cover the region determined by the lowest and highest possible signal speed in both respective directions. Through this it is found that the 2D approximate Riemann solver is given as a superposition of the respective 1D solutions to the Riemann problem. For example, the resulting numerical estimates for the first component of the electric

field

$$\begin{aligned}
& \mathbb{E}_1^{i,j+\frac{1}{2},k+\frac{1}{2}}(t) \\
&= \frac{1}{b_{j+\frac{1}{2}}^\pm c_{k+\frac{1}{2}}^\pm} \left[b_{i,j+\frac{1}{2},k+\frac{1}{2}}^- c_{i,j+\frac{1}{2},k+\frac{1}{2}}^- E_{i,j+1,k+1}^{L_y,L_z} \right. \\
&+ b_{i,j+\frac{1}{2},k+\frac{1}{2}}^- c_{i,j+\frac{1}{2},k+\frac{1}{2}}^+ E_{1,i,j+1,k}^{L_y,R_z} \\
&+ b_{i,j+\frac{1}{2},k+\frac{1}{2}}^+ c_{i,j+\frac{1}{2},k+\frac{1}{2}}^- E_{1,i,j,k+1}^{R_y,L_z} \\
&+ b_{i,j+\frac{1}{2},k+\frac{1}{2}}^+ c_{i,j+\frac{1}{2},k+\frac{1}{2}}^+ E_{1,i,j,k}^{R_y,R_z} \left. \right] \\
&+ \frac{b_{i,j+\frac{1}{2},k+\frac{1}{2}}^+ b_{i,j+\frac{1}{2},k+\frac{1}{2}}^-}{b_{j+\frac{1}{2}}^\pm} \left[B_3^{L_y}{}_{i,j+1,k+\frac{1}{2}} - B_3^{R_y}{}_{i,j,k+\frac{1}{2}} \right] \\
&- \frac{c_{i,j+\frac{1}{2},k+\frac{1}{2}}^+ c_{i,j+\frac{1}{2},k+\frac{1}{2}}^-}{c_{k+\frac{1}{2}}^\pm} \left[B_2^{L_z}{}_{i,j+\frac{1}{2},k+1} - B_2^{R_z}{}_{i,j+\frac{1}{2},k} \right]
\end{aligned} \tag{75}$$

where $L_{y,z}$ ($R_{y,z}$) represents the left- (right-) handed reconstruction polynomial in the y - and z -directions, respectively. Additionally, the abbreviations

$$\begin{aligned}
b_{j+\frac{1}{2}}^\pm &= b_{i,j+\frac{1}{2},k+\frac{1}{2}}^- + b_{i,j+\frac{1}{2},k+\frac{1}{2}}^+; \\
c_{k+\frac{1}{2}}^\pm &= c_{i,j+\frac{1}{2},k+\frac{1}{2}}^- + c_{i,j+\frac{1}{2},k+\frac{1}{2}}^+
\end{aligned} \tag{76}$$

were used. Corresponding expressions are also found for the other electric field components (see, e.g., in Londrillo & Del Zanna 2000; Ziegler 2011a). A derivation extending the finite-volume scheme by Kurganov et al. (2001) to the problem of the electric fields on arbitrary orthogonal grids can be found in Kissmann & Pomoell (2012). When using the HLL Riemann solver, it is highly recommended to use this particular implementation of the constrained transport scheme because it is consistent with the solver for HD variables without the necessity of projecting nonlocal variables. A similar expansion for other Riemann solvers as discussed by Fromang et al. (2006) will be addressed in future extensions of the code.

6.4. Remark I: Grid Singularities

When using non-Cartesian coordinates for the computational grid, the numerical domain may feature coordinate singularities that need a special treatment. We define coordinate singularities as regions where at least one scale factor tends to zero (implying that several vertices of a cell coincide, leading to wedge-shaped or pyramidal cell geometries). Specifically, in a 3D configuration using cylindrical coordinates, the radial grid lines converge onto the vertical z -axis for $\rho \rightarrow 0$, similarly to what is observed in spherical coordinates as $\vartheta \rightarrow \{0, \pi\}$. (In the latter case, there is an additional singularity at $r \rightarrow 0$, where the innermost cells attain the shapes of pyramids whose tips meet at the origin. Because of the lack of applications, this singularity has currently not been implemented into the code, although this is not expected to cause principal difficulties.) Apart from the more severe time-step constraint due to the decreasing azimuthal extent of the grid cells near this axis, this also necessitates a special treatment for the respective axial boundary conditions at ρ_{\min} and $\{\vartheta_{\min}, \vartheta_{\max}\}$. In the following, we briefly describe the related treatment in CRONOS. It is similar to the one used

in the NIRVANA code, for which an extensive discussion is provided by Ziegler (2011a).

For HD problems, the implementation of the corresponding boundary conditions is comparatively simple. For the example of a cylindrical grid, an innermost cell (adjacent to the axis) is given by the indices $(i = 0, j, k)$, with the position of the cell center of $(\Delta\rho/2, \varphi_j, z_k)$ and a radial extent of $\rho \in [0, \Delta\rho]$. The first ghost cell with index $i = -1$ centered at $(-\Delta\rho/2, \varphi_j, z_k)$ has the same physical location as the cell at $(\Delta\rho/2, (\varphi_j + \pi) \bmod(2\pi), z_k)$, and therefore has to reflect the HD quantities of that cell. (There are usually at least two layers of ghost cells, but the procedure for those at $i < -1$ is completely analogous.) This shows that without any additional symmetries, it is necessary to use a grid encompassing the whole azimuthal range. In terms of indices, the first ghost cell reflects the quantities at $j' = (j + N_\varphi/2) \bmod N_\varphi$, where N_φ is the total number of grid cells in the azimuthal direction, which needs to be an even number to allow a direct mapping onto an existing grid position. This leads to the mapping $\bar{u}_{-1,j,k} = \bar{u}_{0,j',k}$ (Ziegler 2011a) for all HD quantities except for the radial and azimuthal velocities u_r and u_φ , for which $\bar{u}_{\{R,\varphi\};-1,j,k} = -\bar{u}_{\{R,\varphi\};0,j',k}$ because the corresponding unit vectors point into the opposite direction for a shift of $\pm\pi$ in azimuth. Table 2 summarizes the corresponding symmetry considerations for all three types of singularities.

Simulations involving a magnetic field pose the additional difficulty that the outward-pointing B component (B_ρ for $\rho = 0$, B_ϑ for $\vartheta \in \{0, \pi\}$, and B_r for $r = 0$) is not defined at cell centers but localized exactly at the singularity, at which the field integration diverges. We describe the procedure adopted in CRONOS for the cylindrical case only, noting that the spherical case is handled completely analogously.

First, all off-axis electric and magnetic field components are treated using the same mapping as described above for HD variables, i.e.,

$$B_{z;-1,j,k-1/2} = B_{z;0,j',k-1/2} \tag{77}$$

$$B_{\varphi;-1,j-1/2,k} = -B_{\varphi;0,j'-1/2,k} \tag{78}$$

$$E_{\rho;-1,j-1/2,k-1/2} = E_{\rho;0,j'-1/2,k-1/2}, \tag{79}$$

while the on-axis components B_ρ , E_φ , and E_z require a dedicated treatment (see Figure 3 for an illustration of the geometrical situation).

For these components, we need to acknowledge that those variables located on the vertical axis are localized at the same position in physical space and therefore need to have a unique value, which in CRONOS is found using an averaging procedure. As long as the on-axis value of E_φ is finite, it has no impact on B_z at $\rho = \Delta\rho/2$ because of the multiplicative factor $h_2 = \rho \rightarrow 0$ in the curl operator in Equation (37). Thus, only E_z and B_ρ need a special treatment for the vertical axis. Of these, the treatment of E_z is rather simple. As discussed in Ziegler (2011a), all on-axis values at a given z position are averaged, and the average thus computed is then used for all of them.

The situation for B_ρ is a little more complicated since a given magnetic field on the vertical axis yields different values of B_ρ for different azimuthal directions. Our treatment of B_ρ differs from the one used by Ziegler (2011a): once all off-axis ghost cells have been updated using the data on the other side of the singularity, the procedure is as follows.

Coord. System	Boundary	Cells to Copy	Minus Sign for
Cylindrical	$\rho = 0$	$[\rho, \varphi, z] \leftarrow [-\rho, \varphi \pm \pi, z]$	ρ, φ components
Spherical	$\vartheta \in \{0, \pi\}$	$[r, \vartheta, \varphi] \leftarrow [r, \vartheta, \pi \pm \varphi]$	r, φ components
Spherical	$r = 0$	$[r, \vartheta, \varphi] \leftarrow [r, \pi - \vartheta, \pi \pm \varphi]$	r, ϑ, φ components

Table 2

Boundary-cell prescription at coordinate singularities. The \pm signs are to be chosen such that the resulting cell exists and is located within the domain.

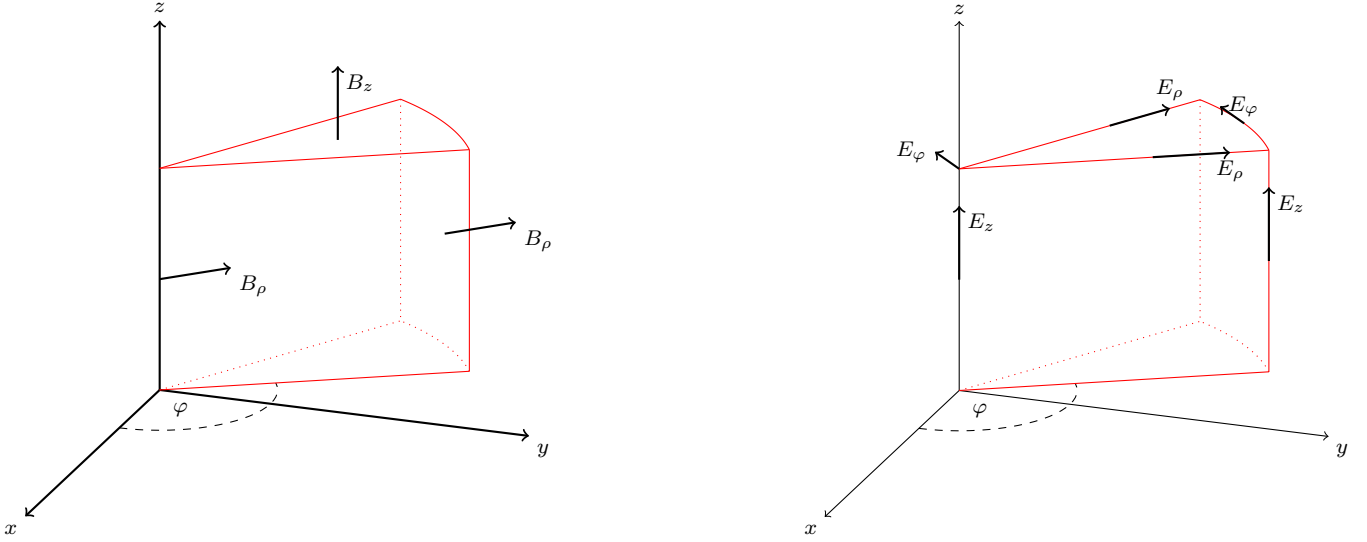


Figure 3. Illustration of the collocation points of the magnetic field (left) and electric field (right) components for a cylindrical cell located at the coordinate axis.

1. First, a pair of horizontal components as projected onto the vertical axis is computed for each φ direction via

$$B_{\rho; -1/2, j, k} = \frac{1}{2} (B_{\rho; 1/2, j, k} + B_{\rho; -3/2, j, k}) \quad (80)$$

$$B_{\varphi; -1/2, j, k} = \frac{1}{4} (B_{\varphi; -1, j-1/2, k} + B_{\varphi; 0, j-1/2, k} + B_{\varphi; -1, j+1/2, k} + B_{\varphi; 0, j+1/2, k}), \quad (81)$$

where the index $i = -1/2$ indicates the position of the axis and those variables located at $i < -1/2$ are given as ghost-cell values as discussed above.

2. These are then transformed to Cartesian coordinates (again for each φ direction) and subsequently averaged according to

$$\langle B_x^0 \rangle_k := \frac{1}{N_\varphi} \sum_j (B_{\rho; -1/2, j, k} \cos \varphi_j - B_{\varphi; -1/2, j, k} \sin \varphi_j); \quad (82)$$

$$\langle B_y^0 \rangle_k := \frac{1}{N_\varphi} \sum_j (B_{\rho; -1/2, j, k} \sin \varphi_j + B_{\varphi; -1/2, j, k} \cos \varphi_j). \quad (83)$$

3. Finally, these unique components are transformed back into cylindrical coordinates, yielding distinct B_ρ components

$$B_{\rho; -1/2, j, k} = \langle B_x^0 \rangle_k \cos \varphi_j + \langle B_y^0 \rangle_k \sin \varphi_j \quad (84)$$

that are used as boundary condition at ρ_{\min} for each φ direction.

This procedure assures that a unique value of the magnetic field at the vertical axis is used, leading to different values of B_ρ for each azimuthal cell. Extending this approach to the case of spherical coordinates (for which the corresponding treatment for the vertical axis is also implemented in CRONOS) is carried out analogously, and will not be discussed here (but see Ziegler 2011a).

6.5. Remark II: Carbuncle Problem

When using either the HLLC or the HLLD solver in a setup where strong shocks that are partly aligned with the underlying grid occur, the user needs to be aware of the possible occurrence of the so-called carbuncle problem. Through this phenomenon, shock waves can become significantly distorted, leading to unphysical results (see, e.g. Quirk 1994).

If this turns out to be an issue for simulations done with the CRONOS code, a cure for this problem is provided as also suggested in Quirk (1994). Here, a threshold parameter as introduced in their Equation (6) is used to determine whether a cell might be prone to the carbuncle instability. Wherever the condition is met, the HLL Riemann solver is used instead of one of the more accurate solvers, because the HLL solver is not prone to the carbuncle phenomenon. While Pandolfi & D'Ambrosio (2001) argue against using two different Riemann solvers, we feel that this is unproblematic with the HLL being closely related to both the HLLC and the HLLD solvers. Thus, CRONOS offers an efficient method to avoid instabilities resulting from the carbuncle phenomenon.

6.6. Remark III: Pressure Positivity

Like the number density n , the thermal energy density e_{th} also needs to be strictly positive in a physically meaningful state. The thermal energy, however, is not a conserved variable. Instead the code solves for the overall energy density and subsequently computes the thermal energy density by subtracting the densities of kinetic and magnetic energies. In situations where the thermal energy is small compared to either the kinetic or the magnetic energy density, unphysical regions of negative thermal energy (implying negative pressure) can arise from simple discretization errors. Whenever this happens, the characteristic speeds become imaginary, forcing the simulation to abort prematurely. To avoid possible related problems, we adopted the scheme introduced by Balsara & Spicer (1999). These authors suggest to use an additional evolution equation

$$\frac{\partial S}{\partial t} + \nabla \cdot (S\mathbf{u}) = 0 \quad (85)$$

for the entropy density $S := p/\rho^{\gamma-1}$. This simple advection equation ensures entropy conservation and is therefore not valid at magnetosonic shocks. Everywhere else, however, it is possible to use conservation of either overall energy or entropy to describe the energy variable. Equation (85) offers the advantage of ensuring positivity of S and thus also of the thermal energy density and the thermal pressure. Thus, the parallel use of Equation (85) alongside Equation (5) allows the energy variable that presumably yields the more accurate result in a given region of the numerical domain at a given instant of time during the simulation to be dynamically chosen.

To decide which description is locally more accurate, Balsara & Spicer (1999) introduced three different switches, which are also applied in CRONOS in the same form. Although the use of this optional scheme comes at the expense of an additional equation to integrate and an additional scalar field to store, it offers the potential to efficiently stabilize a simulation, especially in the case of a low-beta plasma.

7. USING THE CRONOS CODE

7.1. Computational Setup

The CRONOS code is designed to be simple to use and to be easily adapted to advanced problems. User interaction occurs primarily through a parameter file and a module file. The module file has to contain a C++ class that describes the setup of the problem. Such a module file can be based on an example from the suite of standard test cases supplied with CRONOS. The general concept is that the source code contained in the module file supplies all routines and methods that are relevant for a given problem class, while each simulation that uses a given module has its own parameter file, in which specific details such as grid size and resolution, output intervals, or additional custom parameters are provided and read in at the start of a simulation. When standard boundary conditions (in CRONOS, periodic, extrapolating, outflow, and special axis boundaries are supported) are chosen within the parameter file, it is sufficient to specify the initial conditions to run the code.

Apart from the initial conditions and possible user-defined boundary conditions, there is a broad range of additional methods foreseen for the module files that may or may not be used. For example, source terms are handled exclusively via the user module. Apart from that, it is, e.g., possible to set

upper or lower bounds for any variable, which are enforced by the code, or to supply specific flux functions for additional variables that can be integrated using CRONOS.

7.2. Data Output and Analysis

The CRONOS code stores simulation output in hdf5 files (see www.hdfgroup.org). The direct output is two-fold: the complete data are written in full precision at user-defined intervals to allow restarting the code at a given time. To reduce the storage demand, the standard output is also written in reduced precision (float instead of double) at regular output times specified by the user. The data can be investigated by the user employing his preferred analysis tools. There is, however, a small dedicated data analysis package for the CRONOS output files available. Making extensive use of Python's matplotlib library (see Hunter 2007), this package allows slice or line plots to be produced from the data files. This tool, like the code itself, is continuously enhanced to fulfil all upcoming needs by the current user base.

Additionally, CRONOS supports a dedicated movie output (also written as hdf5 files). In this case, only slices from the full 3D data sets are written, and the position of the slice can be set individually for each dimension. The user module also gives some control over the variables written into the movie files, i.e., the user can decide what fields are to be stored in these files. This output mode allows to write data for far more time steps to be written without producing an excessive amount of data. CRONOS also comes with an additional Python tool that can convert these movie output files into actual movies. All plots shown in the subsequent sections where produced using the CRONOS analysis tools.

8. VERIFICATION OF THE CODE

In the following sections, results from a range of numerical tests are discussed to verify the capabilities and reliable operation of the CRONOS code. Both one- and multi-dimensional test simulations using either HD or MHD are investigated, covering both Cartesian and other systems of coordinates.

8.1. Shock-tube Tests

At the beginning, results for several standard shock tube tests are investigated. These consist of two constant states separated by a discontinuity, thus investigating the code's capability to correctly describe the temporal evolution of different Riemann problems. The presence of the discontinuity also reveals whether a numerical scheme is prone to spurious oscillations at such shock waves.

As a first test, we show results of a variation of Sod's shock-tube test (Sod 1978) with stronger gradients in Figure 4. In this setup, we prescribe the initial states on the left and right sides according to

$$[n, p] = \begin{cases} [10, 100] & \text{if } x < 0.5 \\ [1, 1] & \text{if } x \geq 0.5 \end{cases} \quad (86)$$

using an adiabatic index of $\gamma = 1.4$. Results are shown for density and velocity. For this and all subsequent tests, the time step was adapted to yield a CFL number of 0.4. Results were computed using the HLLC Riemann solver together with a second-order reconstruction using the van Leer limiter.

	n_l	p_l	u_l	$B_{\perp,l}$	n_r	p_r	u_r	$B_{\perp,r}$	B_{\parallel}	γ
Sod test	10	100	0	-	1	1	0	-	-	1.4
Einfeldt	1	0.4	-2	-	1	0.4	2	-	-	1.4
Toro	1	1000	-19.59745	-	1	0.01	-19.59745	-	-	1.4
BW	1	1	0	1	0.2	0.1	0	0	1	2

Table 3

Values of density, pressure, velocity, and perpendicular magnetic field in the region left (index l) and right (index r) of the discontinuity for the different shock-tube tests. Additionally, the adiabatic index γ and a possible parallel component of the magnetic field is supplied.

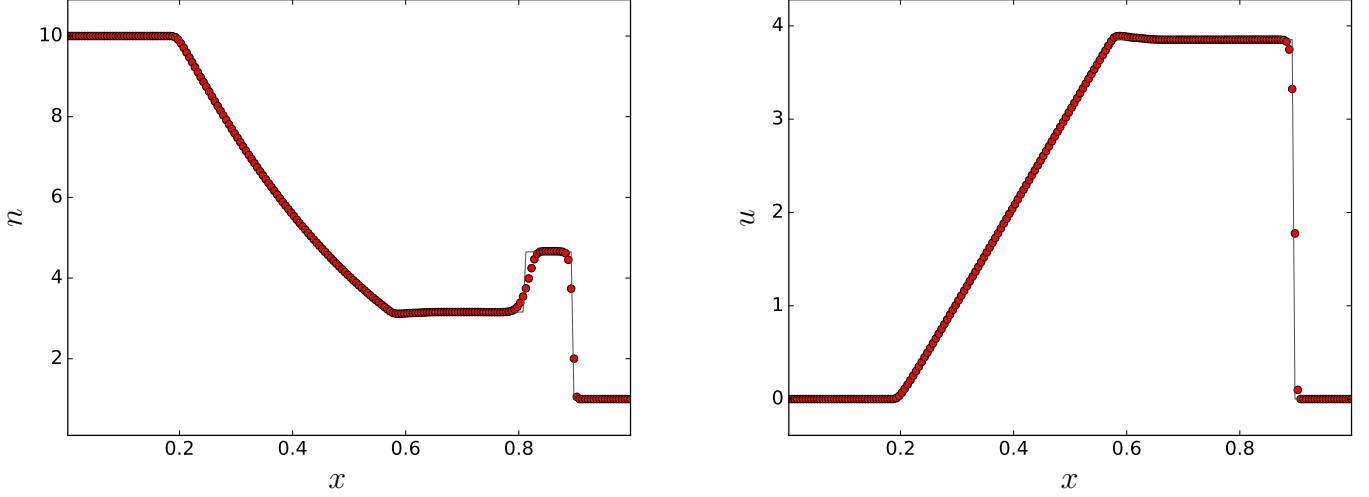


Figure 4. Density (left) and velocity (right) for the modified shock tube test by Sod (1978) at $t = 0.08$ computed with 200 grid cells using the HLLC Riemann solver. The analytical solution is shown as the solid line.

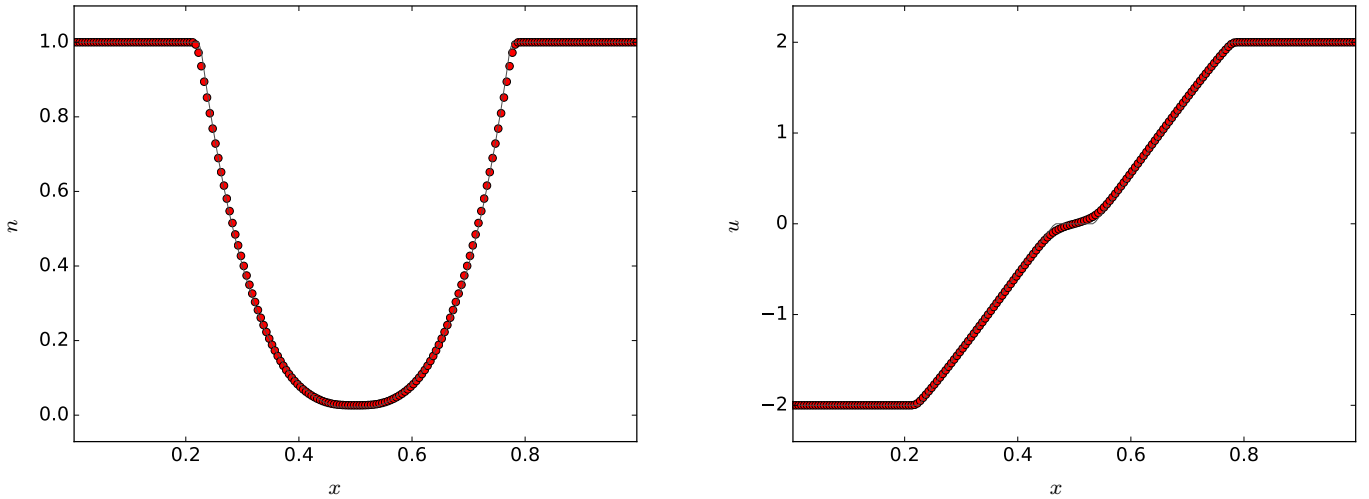


Figure 5. Same as Fig. 4 for test 1-2-0-3 from Einfeldt et al. (1991) at $t = 0.1$.

The test shows that CRONOS can handle strong discontinuities without producing spurious oscillations. Comparison to the analytical solution shows that the resulting Riemann-fan structure is correctly recovered and all wave speeds are apparently correctly implemented.

To check for possible problems associated with strong rarefaction waves, we use test 1-2-0-3 from Einfeldt et al. (1991). The initial conditions for this setup are

$$[n, p, u] = \begin{cases} [1, 0.4, -2] & \text{if } x < 0.5 \\ [1, 0.4, 2] & \text{if } x \geq 0.5. \end{cases} \quad (87)$$

This test is particularly problematic for the Roe solver (see Stone et al. 2008), but does not show any problems for the solvers available in CRONOS. Corresponding results using the same numerical setup as in the first test are shown in Figure 5. The tests did not produce any negative pressure or density values, yielding a good correspondence to the analytical solution.

As the final hydrodynamic shock-tube test, we consider the one used as test 5 in Chapter 10 of Toro (1997) with initial

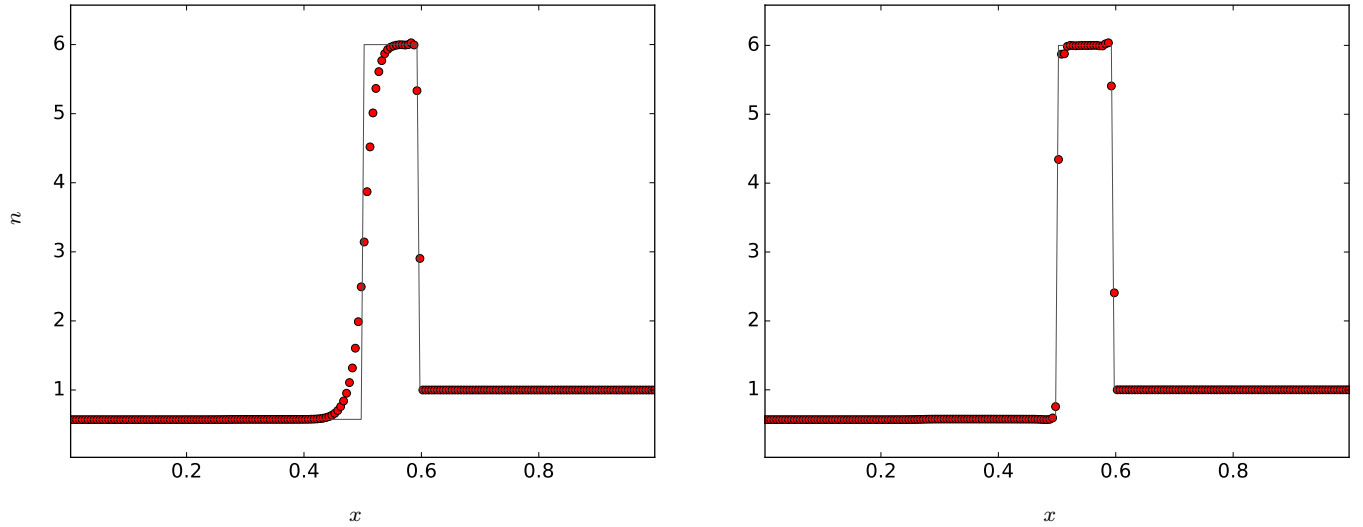


Figure 6. Density for the shock tube test taken from Toro (1997) at $t = 0.24$ computed with 200 grid points using the HLL (left) and the HLLC Riemann solver. The analytical solution is shown as the solid line.

conditions

$$[n, p, u] = \begin{cases} [1, 1000, -19.59745] & \text{if } x < 0.5 \\ [1, 0.01, -19.59745] & \text{if } x \geq 0.5. \end{cases} \quad (88)$$

This setup results in an expanding shock structure with a stationary contact discontinuity. Thus, it is especially suitable for visualizing the advantage of the HLLC Riemann solver compared to the HLL Riemann solver.

Results for this test at time $t = 0.24$ are shown in Figure 6. While the shock wave (the discontinuity on the right side) is nicely recovered by both Riemann solvers, the HLL Riemann solver leads to very diffusive results at the slow-moving contact discontinuity (on the left side). Thus, HLLC is the recommended Riemann solver for the majority of HD problems. Only for cases with prominent carbuncle problems (see Section 6.5) might the use of HLL sometimes be advised.

For all these HD tests, the analytical solution is incorporated in the CRONOS analysis tool. Thus, it can easily be used to verify the different solvers of the code.

While there is no analytical solution available for the MHD shock-tube test by Brio & Wu (1988) (test BW in Table 3), it is used as a common 1D test for MHD codes. Corresponding results are shown in Figure 7. Evidently, the code recovers the correct solution also for MHD Riemann problems, as can be found by a comparison to results from the literature (see, e.g., Brio & Wu 1988; Balsara 1998; Ziegler 2004; Stone et al. 2008, and references therein).

8.1.1. Shu & Osher Test

A test similar to the previously discussed shock-tube tests was introduced by Shu & Osher (1989). In this test a strong shock, propagating to the right, is interacting with a sinusoidal disturbance in density. For this, we use the same setup as described in Shu & Osher (1989), i.e., we use

$$[n, p, u] = \begin{cases} [3.857143, 10.333333, 2.629369] & \text{if } x < -4 \\ [1 + \varepsilon \sin(5x), 1, 0] & \text{if } x \geq -4 \end{cases} \quad (89)$$

with $\varepsilon = 0.2$ in a domain $x \in [-5, 5]$ with $\gamma = 1.4$. Corresponding results are shown in Figure 8 at $t = 1.8$

for resolutions of $N = 3200$ and $N = 400$. Results were computed using the HLLC Riemann solver with the van Leer slope limiter. As also discussed in Shu & Osher (1989), the velocity profile is nicely reproduced at $N = 400$, while the fine-structure in density necessitates a high-resolution setup for a second-order scheme. The implementation of the reconstruction procedure in CRONOS is currently readdressed to allow for the possibility of a higher-order reconstruction.

8.2. Order of the Scheme

To verify the order of the scheme, we ran a series of numerical tests introduced in Ryu & Goodman (1994) and Ryu et al. (1995). These tests employ small-amplitude waves in a 2D domain that are damped by numerical viscosity and resistivity. They allow for an estimate of the corresponding Reynolds numbers according to the prescription in the given papers. We analyzed both HD and MHD setups for different configurations of the numerical solver.

8.2.1. Order of Hydrodynamical Solvers

To investigate the dissipation of the different HD solvers, we determined the decay rates of 2D sound waves as suggested by Ryu & Goodman (1994). For this, we initialized sinusoidal sound waves via

$$\delta v_x = \delta v_y = \delta v_0 c_s \sin(k_x x + k_y y) \quad (90)$$

with wavenumbers

$$k_x = k_y = \frac{2\pi}{L} \quad (91)$$

and $L = 1$. As also discussed in Ryu & Goodman (1994), a nonviscous wave would have an angular frequency of

$$\omega = c_s \sqrt{2} \frac{2\pi}{L}. \quad (92)$$

Thus, the choice $c_s = 1/\sqrt{2}$ leads to one full oscillation per unit time. By simulating up to $t = 10$, we obtain ten such oscillations. This can, e.g., be seen in Figure 9 for an example

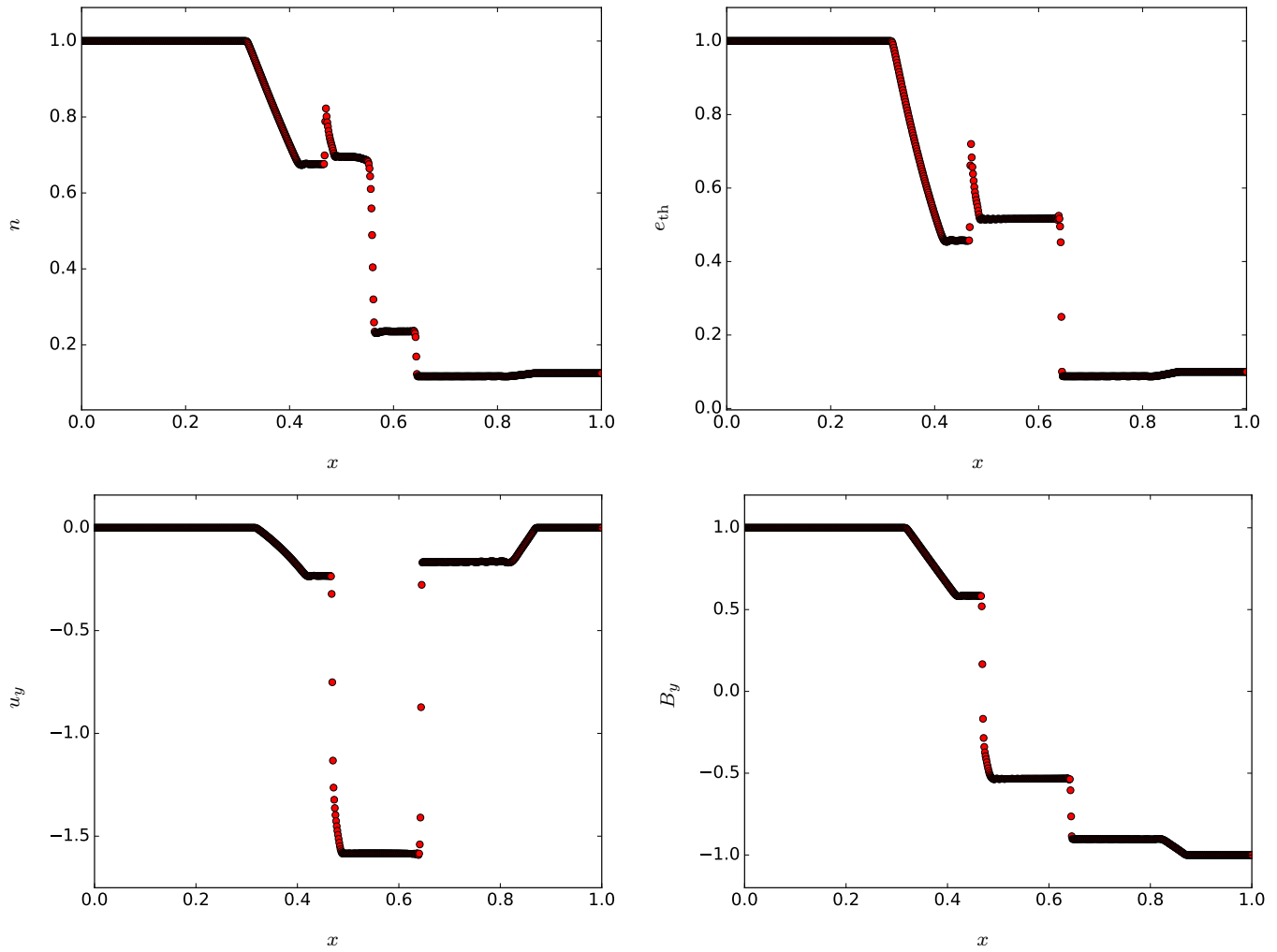


Figure 7. Results for the Brio & Wu (1988) shock-tube test at time $t = 0.1$ computed with 800 grid points. Simulation results are shown for density (upper left), thermal energy (upper right), perpendicular velocity (lower left), and perpendicular magnetic induction (lower right).

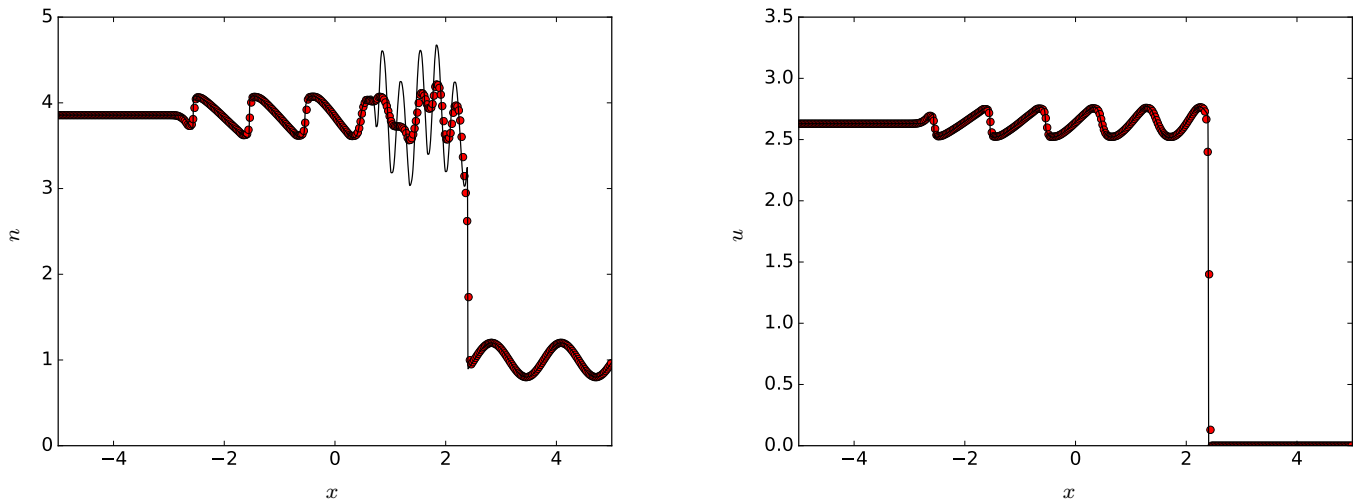


Figure 8. Density (left) and velocity (right) for the Shu & Osher test. The solid line shows very high-resolution results and the circles are for $N = 400$.

with $N = 32$ grid cells in both spatial dimensions. Apparently, ~ 21 peaks occur during the simulation time, each of which reflects one minimum and one maximum during a unit

time. Here, the peak occurs slightly before time $t = 10$ due to the presence of numerical viscosity, which is also reflected by the decrease in amplitude. The logarithmic scale in Figure 9

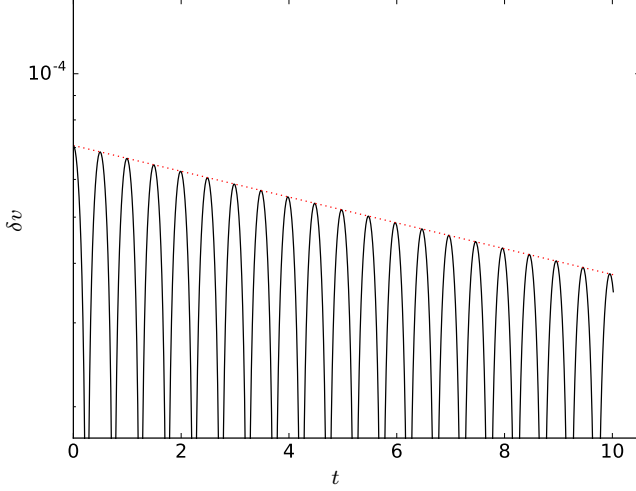


Figure 9. Temporal evolution of the spatial root-mean-square average of the velocity disturbance in the test of the decay of a sound wave. Results are shown for a simulation with 32 grid cells in each dimension using the HLL Riemann solver with the minmod limiter. The red dotted line shows a linear fit to the corresponding exponential decay of the amplitude.

clearly demonstrates the exponential decrease in amplitude.

From the exponential decrease, a decay time scale or a decay rate Γ can be computed. This can be used to determine a Reynolds number according to

$$R_S = \frac{4\pi^2 c_s}{L} \frac{1}{\Gamma}. \quad (93)$$

By plotting this Reynolds number as a function of the number of grid cells for a given simulation, the order of the code can be determined. This is shown on the left side of Figure 10, where the second-order nature is obvious from $R_S \propto N^2$. As expected, the HLLC solver shows somewhat lower viscosity compared to the HLL solver. In both cases, the minmod limiter was used for spatial reconstruction.

8.2.2. Order of MHD Solvers

In a similar fashion, we also determined the dissipation in the MHD solvers of the code. For this we discuss exemplary results for a test of decaying shear Alfvén waves from Ryu et al. (1995). In this case, a velocity disturbance perpendicular to the xy -plane was initialized by

$$\delta v_z = \delta v_0 c_{A,k} \sin(k_x x + k_y y), \quad (94)$$

with $c_{A,k}$ the component of the Alfvén speed along the propagation direction of the wave given by $\mathbf{k} = (k_x, k_y)$. Here, k_x and k_y were chosen to be identical as in the test for decaying sound waves. For very low viscosity, the frequency of the wave is

$$\omega = \pm c_{A,k} k \quad \text{with} \quad k = \sqrt{k_x^2 + k_y^2} = \sqrt{2} \frac{2\pi}{L}. \quad (95)$$

Thus, by choosing $c_A = 1$, we have $c_{A,k} = 1/\sqrt{2}$, also leading to a full oscillation per unit time. Results for this setup were computed using the HLL and the HLLD Riemann solvers. Like in the HD test, an effective Reynolds number was computed via

$$R_A = \frac{8\pi^2 c_{A,k}}{L} \frac{1}{\Gamma}, \quad (96)$$

where Γ is the measured decay rate of the wave. The resolution dependence of the Reynolds number is shown in Figure 10. Also, the MHD part of the code is apparently of second order. In this particular test, the HLLD solver is about a factor of ~ 3 less dissipative than the HLL Riemann solver, reflecting the improved implementation of Alfvén waves by the former.

8.3. Test of Multi-fluid Interaction

While many well-established test cases exist for the dynamics of single neutral or conducting fluids, corresponding test scenarios for the mutual interaction of more than one fluid are relatively sparse. In order to quantitatively examine CRONOS' ability to handle this important class of problems, we draw inspiration from Section 8.2 and consider the two-fluid equations which describe a partially ionized hydrogen plasma, as laid out and derived by Zaqarashvili et al. (2011). When ignoring the Hall term and magnetic resistivity, the equations for number density, momentum density, and magnetic field read

$$\partial_t n_i + \nabla \cdot (n_i \mathbf{V}_i) = 0 \quad (97)$$

$$\partial_t n_n + \nabla \cdot (n_n \mathbf{V}_n) = 0 \quad (98)$$

$$\begin{aligned} \partial_t (m_i n_i \mathbf{V}_i) + \nabla \cdot (m_i n_i \mathbf{V}_i \mathbf{V}_i) + \nabla p_{ie} \\ = \mathbf{J} \times \mathbf{B} + \frac{\alpha_{en}}{en_e} \mathbf{J} - \alpha_{in} (\mathbf{V}_i - \mathbf{V}_n) \end{aligned} \quad (99)$$

$$\begin{aligned} \partial_t (m_n n_n \mathbf{V}_n) + \nabla \cdot (m_n n_n \mathbf{V}_n \mathbf{V}_n) + \nabla p_n \\ = -\frac{\alpha_{en}}{en_e} \mathbf{J} + \alpha_{in} (\mathbf{V}_i - \mathbf{V}_n) \end{aligned} \quad (100)$$

$$\begin{aligned} \partial_t \mathbf{B} - \nabla \times (\mathbf{V}_i \times \mathbf{B}) \\ = \nabla \times \left(\frac{\nabla p_e}{en_e} \right) + \nabla \times \left(\frac{\alpha_{en} (\mathbf{V}_i - \mathbf{V}_n)}{en_e} \right), \end{aligned} \quad (101)$$

in which $[m_\alpha, n_\alpha, \mathbf{V}_\alpha, p_\alpha]_{\alpha \in \{i, e, n\}}$ denote the respective particle masses, number densities, velocities, and pressures of ions (i), electrons (e), and neutral atoms (n). e is the elementary charge, while α_{in} and α_{en} are the coefficients of friction between species.

8.3.1. Simplifying Assumptions

For our test, we strive to use the simplest setup that still allows Alfvén waves to propagate. Specifically, we consider a hydrogen plasma ($m_e \ll m_i \Rightarrow m_n = m_i$) which is partially ionized and make use of quasi-neutrality ($n_e = n_i =: n$) and an isothermal equation of state with equal temperatures for all species ($T_e = T_i = T_n =: T = \text{const.}$), such that

$$p_e = nkT \quad \text{and} \quad p_{ie} = p_i + p_e = 2nkT. \quad (102)$$

Under these conditions, the first term on the right-hand side of the induction equation (101) is proportional to $\nabla \times [(\nabla n)/n] = \nabla \times [\nabla (\ln n)] = \mathbf{0}$ and thus vanishes.

With normalization constants

total number density	$n_0 := (n_{i0} + n_{n0})$
Alfvén speed	$c_A := B_0 / \sqrt{\mu_0 m_i n_0}$
proton gyration timescale	$t_0 := m_i / (eB_0)$
length unit	$L_0 := c_A / \nu_{in}$
collision frequency	$\nu_{in} := \alpha_{in} / (m_i n_0)$,

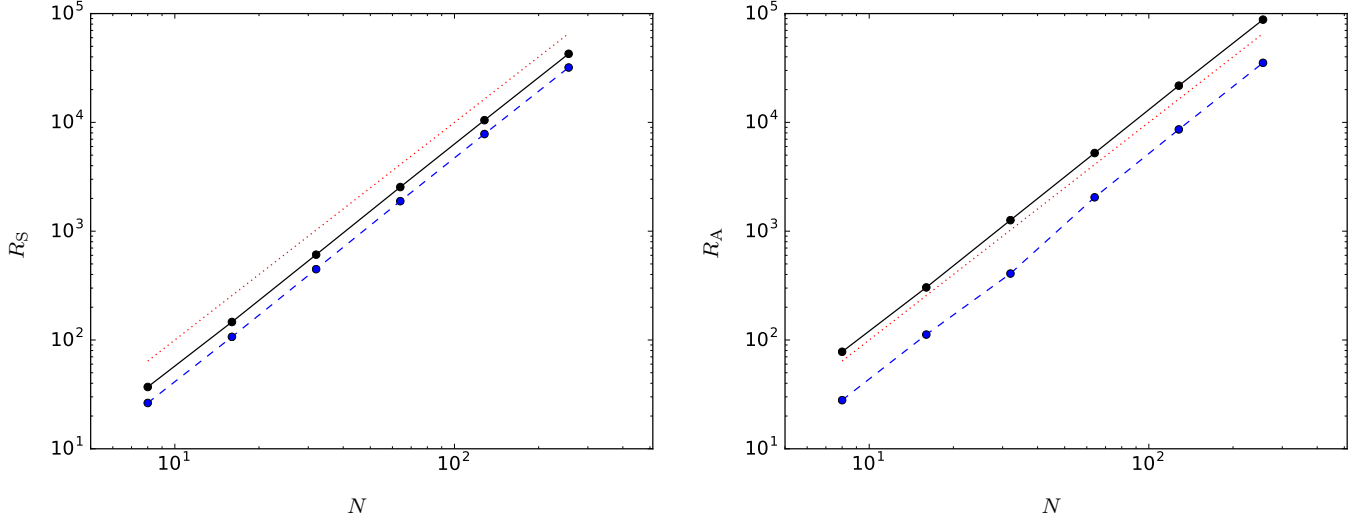


Figure 10. Reynolds number as a function of the number of grid cells N . Results are shown for decaying sound waves (left) and decaying shear-Alfvén waves (right). The black solid lines indicate results obtained using the HLL Riemann solver, and the dashed blue ones show results with the HLLC or the HLLD Riemann solver, respectively. The red dashed line indicates a N^2 dependence to guide the eye.

new definitions

$$\hat{n}_{i,n} := n_{i,n}/n_0 \quad (103)$$

$$\hat{\mathbf{u}}_{i,n} := \mathbf{V}_{i,n}/c_A \quad (104)$$

$$c_n := \sqrt{p_n/(m_i n)} = \sqrt{kT/m_i} \quad (105)$$

$$c_i := \sqrt{p_{ie}/(m_i n)} = \sqrt{2kT/m_i} \quad (106)$$

$$\beta := \alpha_{en}/\alpha_{in} \ll 1 \quad (107)$$

and ignoring collisions between electrons and neutrals (i.e., setting $\beta = 0$), we arrive at

$$\partial_{\hat{t}} \hat{n}_i + \hat{\nabla} \cdot (\hat{n}_i \hat{\mathbf{u}}_i) = 0 \quad (108)$$

$$\partial_{\hat{t}} \hat{n}_n + \hat{\nabla} \cdot (\hat{n}_n \hat{\mathbf{u}}_n) = 0 \quad (109)$$

$$\begin{aligned} \partial_{\hat{t}} (\hat{n}_i \hat{\mathbf{u}}_i) + \hat{\nabla} \cdot (\hat{n}_i \hat{\mathbf{u}}_i \hat{\mathbf{u}}_i) + (c_i/c_A)^2 \hat{\nabla} \hat{n}_i \\ = \hat{\mathbf{J}} \times \hat{\mathbf{B}} - (\hat{\mathbf{u}}_i - \hat{\mathbf{u}}_n) \end{aligned} \quad (110)$$

$$\begin{aligned} \partial_{\hat{t}} (\hat{n}_n \hat{\mathbf{u}}_n) + \hat{\nabla} \cdot (\hat{n}_n \hat{\mathbf{u}}_n \hat{\mathbf{u}}_n) + (c_n/c_A)^2 \hat{\nabla} \hat{n}_n \\ = \hat{\mathbf{u}}_i - \hat{\mathbf{u}}_n \end{aligned} \quad (111)$$

$$\partial_{\hat{t}} \hat{\mathbf{B}} - \hat{\nabla} \times (\hat{\mathbf{u}}_i \times \hat{\mathbf{B}}) = \mathbf{0} \quad (112)$$

and $\hat{\mathbf{J}} = \hat{\nabla} \times \hat{\mathbf{B}}$ as usual. (As before, normalized variables and operators are marked with a hat.) We see that in this simple situation, only the ionized fluid couples to the magnetic field (in the usual way), and both fluids only interact through friction terms in their momentum equations. Equations (108)–(112) represent the equations that have been implemented for this particular test.

8.3.2. Properties of Multifluid Alfvén Waves

When linearizing the two-fluid equations (108)–(112), assuming the unperturbed magnetic field to be oriented along z and the fluctuations of \mathbf{u} and \mathbf{B} to point into the invariant

($\partial_y = 0$) y -direction, we obtain

$$\frac{\partial \hat{u}_{i,y}}{\partial \hat{t}} = \frac{\partial \hat{B}_y}{\partial z} - (\hat{u}_{i,y} - \hat{u}_{n,y}) \quad (113)$$

$$\frac{\partial \hat{u}_{n,y}}{\partial \hat{t}} = \hat{u}_{i,y} - \hat{u}_{n,y} \quad (114)$$

$$\frac{\partial \hat{B}_{i,y}}{\partial \hat{t}} = \frac{\partial \hat{u}_{i,y}}{\partial z}. \quad (115)$$

as the dimensionless version of Equations (48)–(52) in Zaqarashvili et al. (2011). (Since only dimensionless quantities are considered in the remainder of the paper, we again omit the hats from here onwards for simplicity of notation, as well as the y index of $\hat{u}_{i,n,y}$ since this is the only non-zero component anyway.) The requirement that waves of type

$$\frac{u_i}{u_i^0} = \frac{u_n}{u_n^0} = \frac{B_y}{B_y^0} = \exp[i(kz - \omega t)] \quad (116)$$

represent solutions to Equations (113)–(115) leads to a dispersion relation

$$\xi_i \xi_n \omega^3 + i\omega^2 + (i - \xi_n \omega) = 0 \quad (117)$$

(with $\xi_{i,n} = n_{i,n}/n_0$ denoting the ionized and neutral density fractions), as well as to the two conditions

$$u_i^0 = -B_y^0 [\omega/k] \quad (118)$$

$$u_n^0 = -B_y^0 [\omega/k + i(k - \xi_i \omega^2/k)], \quad (119)$$

which constrain the initial amplitudes. Unlike one-fluid Alfvén waves in a fully ionized medium, which experience no damping at all, the corresponding two-fluid waves are damped by collisions between ions and neutrals, indicated by the fact that the dispersion relation (117) has only complex roots.

Note that since Zaqarashvili et al. (2011) “normalize” the wave frequency ω to $k c_A$ rather than ν_{in} , what they refer to as normalized frequency ϖ is actually a dimensionless velocity. Consequently, their dispersion relation (42) may be obtained from Equation (117) via $\varpi = \omega/k$, and the single-fluid version of their dispersion relation (Equation (44) in that paper)

for a partially ionized plasma (Braginskii 1965) reads

$$\omega^2 + (i\xi_i^2\omega - 1)k^2 = 0. \quad (120)$$

8.3.3. Testing Procedure

The test consists of a sequence of (in this case) 20 individual simulations, each one using waves of a specific wavenumber. A one-dimensional periodic grid of 400 cells is initialized according to

$$n_{i,n}|_{t=0} = \xi_{i,n} \quad (121)$$

$$u_{i,n}|_{t=0} = U_{i,n}^0 \cos(kz + \varphi_{i,n}) \quad (122)$$

$$B_z|_{t=0} = 1 \quad (123)$$

$$B_y|_{t=0} = B_y^0 \cos(kz) \quad (124)$$

with $\xi_i = \xi_n = 0.5$ and $B_y^0 = 0.05$, and $U_{i,n}^0$ denoting the real-valued amplitude of $u_{i,n}^0$. In order to satisfy Equations (118) and (119), amplitudes and phase differences are determined from these constraints via a splitting of $\omega = \omega_R + i\omega_I$ into real and imaginary parts, and

$$\begin{aligned} \text{Re}(u_i) &= \text{Re}[u_i^0 \exp(ikz)] \\ &= \text{Re}[-B_y^0(\omega_R + i\omega_I)/k][\cos(kz) + i\sin(kz)] \\ &= -(B_y^0/k)[\omega_R \cos(kz) - \omega_I \sin(kz)] \\ &= \underbrace{-(B_y^0|\omega|/k)}_{U_i^0} \cos[kz + \underbrace{\arctan(\omega_I/\omega_R)}_{\varphi_i}]. \end{aligned} \quad (125)$$

Similarly, we obtain

$$U_n^0 \sin \varphi_n = -B_y^0 [(k\omega_I + 1)\omega_R] \quad (126)$$

$$U_n^0 \cos \varphi_n = -B_y^0 [k(\omega_R^2 - \omega_I^2)/2 - \omega_I - k] \quad (127)$$

for the neutral fluid. ω_R and ω_I are found from a look-up table containing the numerically determined roots of the dispersion relation (117).

The extent of the computational volume in z chosen as $[0, 2\pi/k]$, thus covering exactly one full wavelength. The simulation is halted at $t_{\text{end}} = 10/k$, which is roughly sufficient for two full periods in all cases. At 50 equidistant time frames, the amplitudes $A_k(t)$ and positions $z_k(t)$ of B_y 's maximum are noted, and the values of the damping constant Γ_k and the phase velocity v_k are found by fitting formulas

$$z_k(t) = z_k(0) + v_k t \quad (128)$$

$$A_k(t) = A_k(0) \exp(-\Gamma_k t) \quad (129)$$

to the data. This procedure is repeated for k values from 0.5 to 10 in steps of 0.5.

8.3.4. Test Results

Figure 11 presents the results for v_k and Γ_k thus obtained, and compares them to their respective theoretical predictions ω_R/k and $-\omega_I$, demonstrating excellent agreement. For illustrative purposes, Figure 12 additionally compares the amplitude decay $t \mapsto A_k(t)$ of a standard one-fluid Alfvén wave (exhibiting only very small damping induced by numerical resistivity) to two otherwise identical two-fluid waves, for one

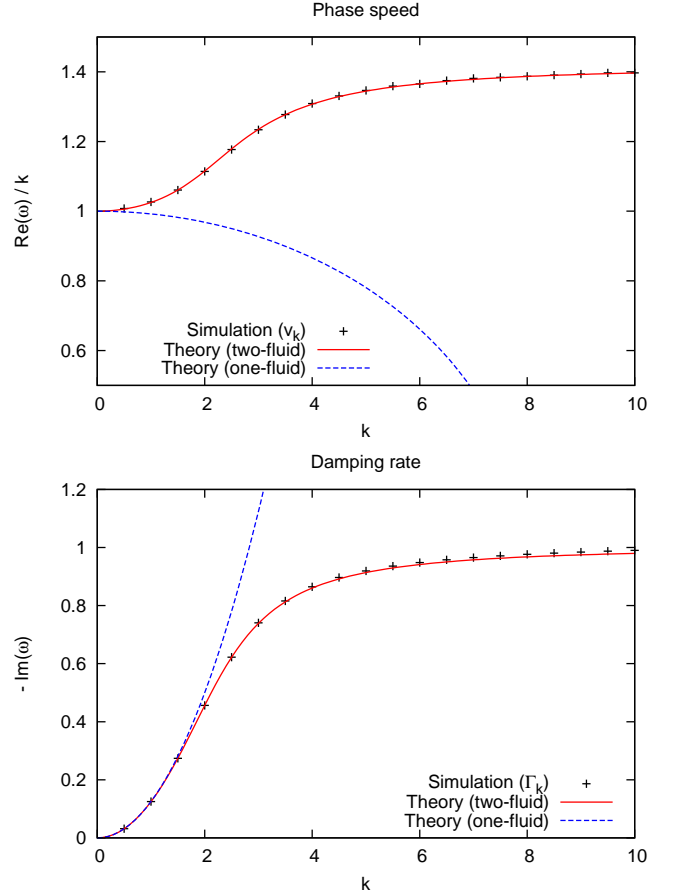


Figure 11. Phase speed (top) and damping rate (bottom) as a function of wavenumber k for two-fluid Alfvén waves. The solid red curves mark the expected values according to Equation (117), while the blue dashed lines show the behavior expected for one-fluid Alfvén waves in a partially ionized plasma according to Equation (120). The latter is included to facilitate comparison to Figure 1 in Zaqarashvili et al. (2011).

of which the initial amplitude and phase shift have not been properly adjusted. The emergent oscillatory behavior clearly demonstrates that this wave is not a valid solution of the plain-wave equations (113)–(115), highlighting the paramount importance of properly chosen initial conditions.

8.4. Parker-wind Test

Motivated by the discussion by Biermann (1951) that the solar atmosphere should comprise a radial gas outflow, Parker (1958) laid the theoretical foundations for a mathematical description of such a solar wind. By assuming an isothermal, spherically symmetric solar atmosphere, he derived a semi-analytical solution for the wind's expansion velocity. This solution of the expanding solar wind is fully determined by specifying the mass of the Sun and the temperature of its atmosphere. Thus, the related setup is well suited as a 1D test case, determining the ability of the code to recover the steady-state solution of an expanding solar atmosphere.

The test features an isothermal plasma with the gravitational force of the Sun as an additional source term. Initially the temperature is set to $T = 3 \cdot 10^6$ K. Radial velocity is initialized by a linear increase up to twice the speed of sound:

$$v_r = c_s \begin{cases} r/r_c & \text{if } r < 2r_c \\ 2 & \text{else,} \end{cases} \quad (130)$$

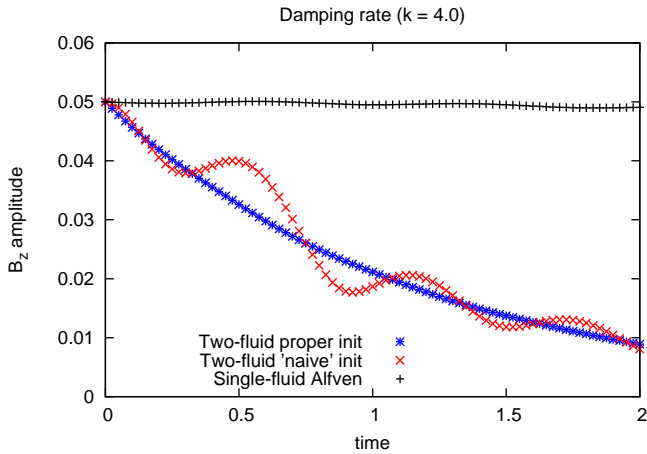


Figure 12. Temporal evolution of a wave’s B_z amplitude for a two-fluid Alfvén wave whose initial condition is set by Equations (125)–(127) (blue stars) and the same wave but initialized like a one-fluid wave, i.e., with equal phases and amplitudes for both u_z and B_z (red \times) compared to a standard one-fluid Alfvén wave in a fully ionized medium (black $+$).

where the critical radius is

$$r_c = \frac{GM_\odot}{2c_s^2} \quad (131)$$

with the solar mass M_\odot , the gravitational constant G , and the speed of sound c_s . As an illustration, we use a nonlinear radial grid in this test. The position of cell interfaces is given by

$$r_i = r_b \left(\frac{r_e}{r_b} \right)^{i/N}, \quad (132)$$

where i is the index of the given cell interface and $N = 65$ their total number. Here, we used $r_b = 1$ and $r_e = 5$ as the lower and upper boundary of the radial grid. At the lower boundary, the radial velocity was linearly interpolated, while the density was prescribed by demanding the chosen mass-loss rate of $2.5 \cdot 10^{-14} M_\odot/\text{year}$. At the outer boundary, extrapolating boundary conditions were used for all variables.

The solution was evolved until the code arrives at a steady state with the results shown in Figure 13. For the velocity the analytical solution is shown together with the simulation results, demonstrating that the code arrives at the correct solution. The effect of the nonlinear grid is clearly visible through the smaller cell size near the solar surface at $r = 1$. This test demonstrates the capability of the code to recover the correct solution also for smooth flows and especially when using a nonlinear grid. Use of such a grid was particularly important, e.g., for the simulation of line-driven winds of early-type stars as discussed in Kissmann et al. (2016), where the launching of the stellar winds shows much steeper gradients than for a pressure driven stellar wind.

8.5. Multidimensional Tests

To test the capability of the code in the context of multidimensional MHD problems we use a range of established numerical tests. While the majority of these tests does not possess an analytical solution, they are well represented in the literature. Thus, the results can be compared to those produced using other numerical methods.

8.5.1. Orszag-Tang Vortex

A standard 2D test to check the ability of a code to handle MHD turbulence is the Orszag-Tang vortex (Orszag & Tang 1979). This test is widely used in the literature, thus allowing a comparison to results obtained using other simulation frameworks (see, e.g., Londrillo & Del Zanna 2000; Stone et al. 2008). The initial conditions use homogeneous density and pressure with respective constant values $\rho_0 = 25/(36\pi)$ and $p_0 = 5/(12\pi)$. Turbulence is initiated by introducing a large-scale disturbance for the velocity and the magnetic vector potential via

$$\begin{aligned} v_x &= -\sin(2\pi y); & v_y &= \sin(2\pi x); \\ A_z &= \frac{B_0}{4\pi} \cos(4\pi x) + \frac{B_0}{2\pi} \cos(2\pi y) \end{aligned} \quad (133)$$

with $B_0 = 1/\sqrt{4\pi}$. For the adiabatic exponent, we use $\gamma = 5/3$. The simulations are run for a simulation box with size $L_x = L_y = 1$ using 192 grid cells in each dimension. Results are shown in Fig. 14 at time $t = 0.5$.

The turbulence produced in this configuration is related to different MHD modes and accompanying shock waves. Thus, a code’s inability to handle any of these correctly should show up in a comparison to the results by other codes. Additionally, a divergence constraint $\nabla \cdot \mathbf{B} = 0$ not being fulfilled by the code would also show up in this test. A visual comparison, e.g., to Figure 10 of Londrillo & Del Zanna (2000) or Figure 24 of Stone et al. (2008) shows excellent qualitative agreement to results produced using other numerical codes.

8.5.2. Magnetic Rotor Problem

Here, we use the well-established magnetic rotor problem to verify the analogy of the results computed on a Cartesian and on a cylindrical grid. The magnetic rotor problem was introduced by Balsara & Spicer (1999) as a tests for the correct description of torsional Alfvén waves. This problem uses a rapidly rotating dense cylinder in an otherwise homogeneous background. The initial magnetic field is oriented perpendicular to the rotation axis, where we prescribe a magnetic field in the x -direction with the angular momentum in the z -direction.

In our 2D setup, we use the specific initial conditions given in Kissmann & Pomoell (2012) with an adiabatic index $\gamma = 1.4$. A comparison of results computed using Cartesian and cylindrical coordinates is shown in Figure 15. Both simulations use the same numerical setup, i.e., they were computed using the HLLD Riemann solver with the minmod limiter. Both grids were configured to yield a comparable spatial resolution. The Cartesian mesh covers an extent $x, y \in [-0.5, 0.5]$ with $N_x \times N_y = 512 \times 512$ cells. The cylindrical mesh covers $\rho \in [0, 0.55]$ with 256 cells and uses 564 cells in the φ direction.

It is obvious from Figure 15 that there are no significant differences between the results computed using different grid setups. Also, a comparison to the results by Ziegler (2011a) shows excellent agreement.

8.5.3. Current-sheet Test

To investigate the behavior of the code in the presence of a magnetic current sheet, we adopted a test suggested by Hawley & Stone (1995) in which current sheets are subjected to

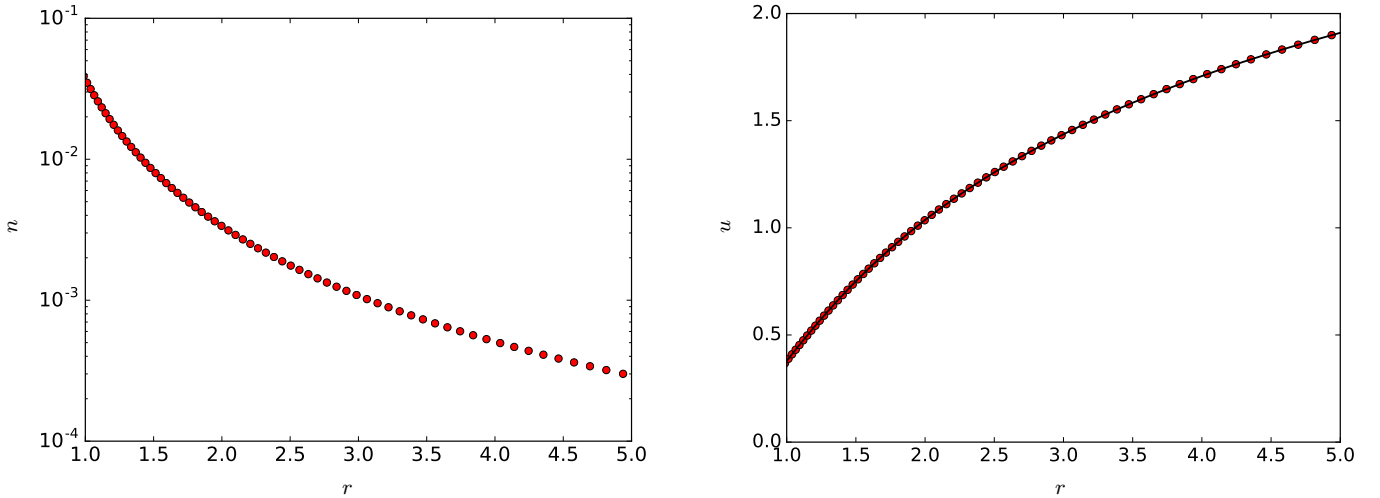


Figure 13. Converged steady-state solution for the Parker-wind test. Results obtained using CRONOS are shown as red circles with number density n (using a normalization of $n_0 = 10^{14} \text{ m}^{-3}$) on the left and velocity (as multiples of the isothermal speed of sound) on the right. Additionally, the analytical solution for the velocity is shown on the right as the solid line. Distances are given in units of the solar radius.

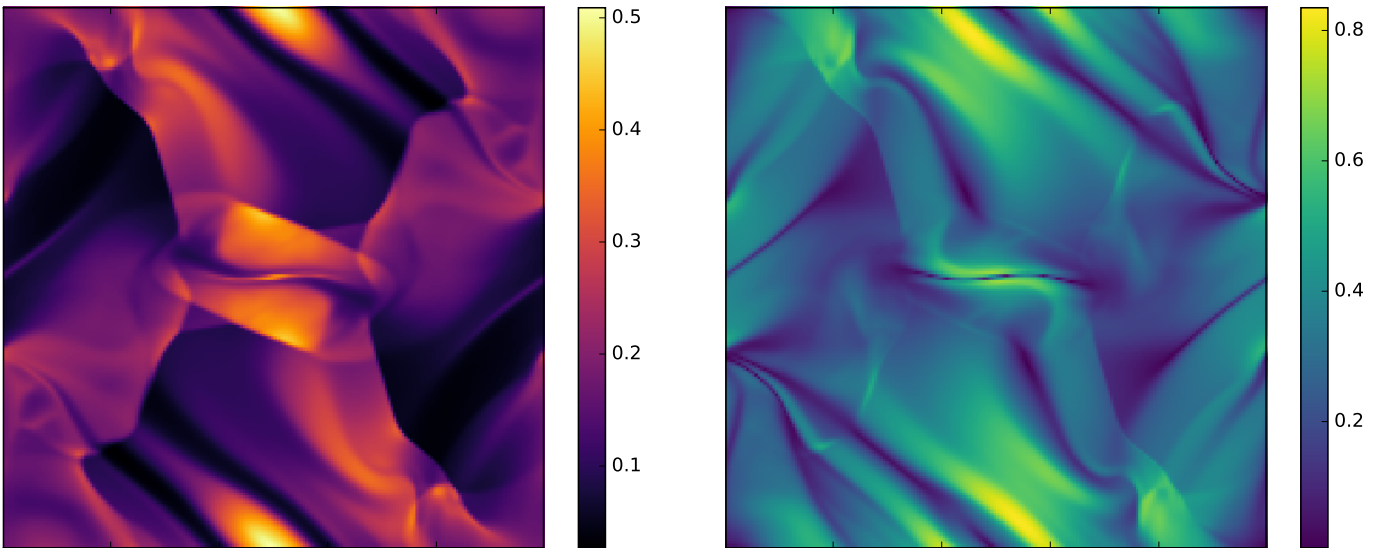


Figure 14. Pressure (left) and absolute value of magnetic field (right) for the Orszag-Tang vortex test at time $t = 0.5$.

a small perpendicular velocity disturbance. In the periodic numerical domain with the extent $(x, y) \in [0, 2]^2$, two parallel current sheets, at which the magnetic field pointing in the y -direction reverses its direction, are placed at $x = 0.5$ and $x = 1.5$. In our implementation, we used the specific setup discussed in Gardiner & Stone (2005) and Fromang et al. (2006). In particular, we used a value of $\beta = p_0/e_{\text{mag}} = 0.2$, leading to strong overpressure in regions where reconnection occurs. For the velocity disturbance, we used $v_x = A \sin(\pi y)$ with $A = 0.1$. The constant background quantities were set to $\rho_0 = 1$, $p_0 = \beta/2$, and $B_0 = 1$. The problem was solved on an $N_x \times N_y = 256 \times 256$ grid.

While there is again no analytical solution to this test, results can be compared to those computed using other numerical codes. The results are sensitive to the specific implementation of the scheme, because the dynamics is driven by the ongoing magnetic reconnection, and this depends on the extent of numerical diffusivity that is present in the scheme. We indeed found that the results of the test critically depend on

the choice of the Riemann solver and the slope limiter. This test is very sensitive to any errors in the implementation of the constrained-transport scheme and helped in optimizing the implementation of the magnetic field evolution in CRONOS.

The results shown in Figure 16 were computed with the HLLD Riemann solver together with the van Leer slope limiter. The dynamics of the magnetic field in the CRONOS simulations are very similar to those found by Fromang et al. (2006), indicating that the HLLD Riemann solver performs similarly to the Roe solver that is used in their study. Also, in the CRONOS simulations, the breaking of the flow symmetry appears later than in the simulations shown in Gardiner & Stone (2005). This relates to the different numerical diffusivity, where the most relevant difference to Gardiner & Stone (2005) is their use of a piecewise quadratic reconstruction, while in CRONOS the reconstruction is of second order. In Figure 16 we also show that the symmetry in the simulations done with CRONOS is broken at later times, where the active merging of magnetic islands is visible at $t = 10$.

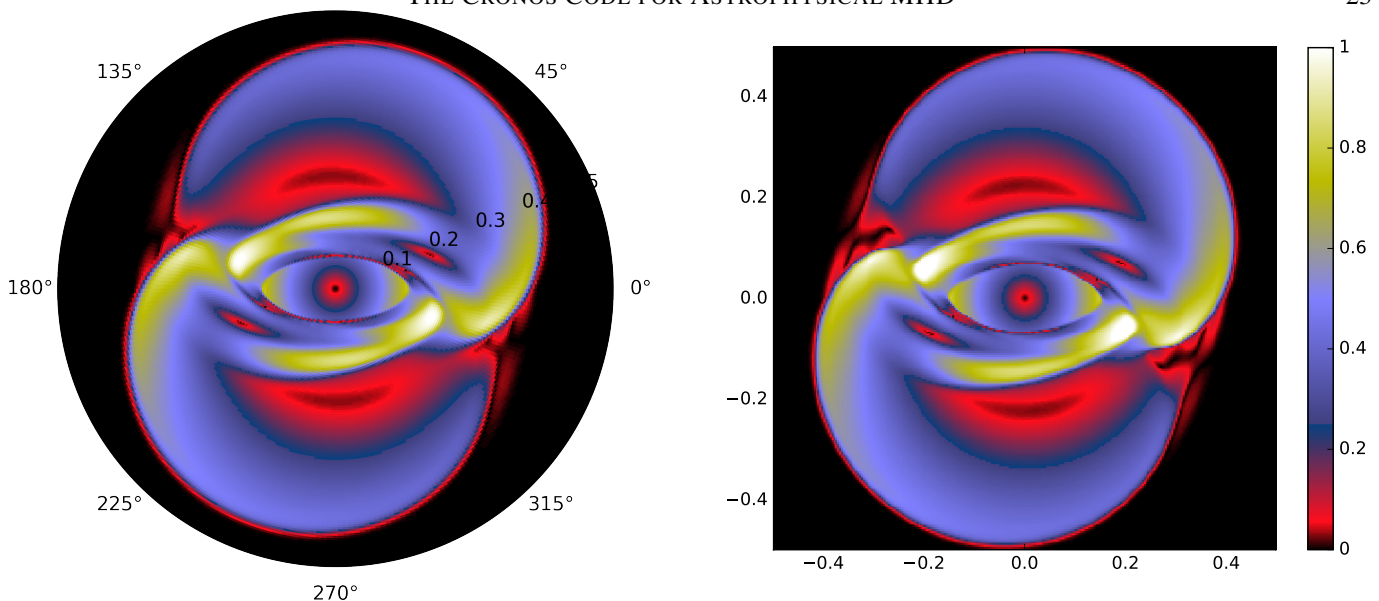


Figure 15. Absolute value of velocity for the magnetic rotor problem at time $t = 0.18$. Results are shown for a cylindrical (left) and a Cartesian mesh (right).

8.5.4. Alfvén Wing Test

When a magnetic field advected with a fluid encounters a localized obstacle, Alfvén waves are excited and propagate along the magnetic field lines away from the obstacle. This effect has been closely investigated by Drell et al. (1965) and Neubauer (1980). While it is physically relevant for different planetary bodies (Kopp & Schröder 1998), it also provides a useful test for a numerical code. Considering that Alfvén waves propagate along the magnetic field with the Alfvén velocity c_A while the magnetic field is simultaneously advected with the fluid velocity \mathbf{u} shows that in a configuration where $\mathbf{B} \perp \mathbf{u}$, the waves propagate at an angle $\vartheta_A = \arctan(M_A^{-1})$ (Ridley 2007) relative to the direction of the background flow, where $M_A = u/c_A$ is the Alfvénic Mach number. Thus, the critical aspects of such an Alfvén wing test are the correct reproduction of ϑ_A for a given background plasma configuration and also the correct expansion of the Alfvén wing structure.

Correspondingly, the test features a homogeneous plasma flow with a superimposed homogeneous magnetic field perpendicular to the flow velocity. An obstacle is introduced by a local modification of the flow velocity via

$$\mathbf{u}(\mathbf{r}, t)^* = \mathbf{u}(\mathbf{r}, t) [1 - \min(10t, 1) \times (1 - \tanh(4 \max(4d - 1, 0)))], \quad (134)$$

where $d = \|\mathbf{r} - \mathbf{x}\|$ is the distance from the center \mathbf{x} of the disturbance (see also Kleimann et al. 2009) and t is time in numerical units. Consequently, the flow velocity within a region $d < 1/4$ around the position of the obstacle will vanish for $t > 0.1$. By setting v_A in our simulations to the value of the background flow velocity, the Alfvén waves are expected to travel at an angle of 45° relative to the background flow.

This problem was solved on a Cartesian and a spherical mesh. For the Cartesian mesh, an extent of $x, y, z \in [-16, 16]$ with 256 cells was used in each dimension. The spherical mesh is given as $r \in [1, 31]$, $\vartheta \in [\pi/4, 3\pi/4]$, and $\varphi \in [-\pi/4, \pi/4]$, where 256 cells in the radial and 128 cells in each angular dimension were used, leading to a similar spatial resolution at the center of the numerical domain. Here, a

configuration with the background flow in the positive z and the magnetic field in the x -direction was investigated. Thus, the Alfvén wings are expected to occur in the xz -plane. The disturbance was placed at $\mathbf{x} = (18, 0, -5)$.

Simulation results for both configurations are shown in Figure 17, where $|\mathbf{u}|$ is shown in the $y = 0$ or $\varphi = 0$ plane, respectively. Apparently, the direction of the wings is correctly captured by the code. For our choice of $c_A = |\mathbf{u}| = 1$, the extent of the wings has to be $\Delta x = \Delta z = 8$ in the x - and the z -directions; this is also correctly reproduced. Additional configurations for this test have been investigated by Kissmann & Pomoell (2012), also showing the correct behavior. The slight differences between the results computed on a Cartesian and a spherical mesh can be attributed to the radially increasing angular extent of the grid cells on the spherical mesh.

8.6. Code Performance

CRONOS has been successfully run on a variety of different platforms using up to ~ 1000 computing cores. The scaling performance on a SGI Altix UV 1000 system with Xeon E7-8837 processors is shown in Figure 18. In this study, we investigated strong scaling for an HD and an MHD test, each with a 3D grid of 256^3 cells. For the HD test, we used the 3D Sedov-explosion test (see Section 9 for a discussion of the 2D Sedov-explosion test), and for the MHD test, we used the Alfvén wing test introduced in Section 8.5.4. We find satisfactory results for strong scaling with CRONOS.

To quantify the performance of CRONOS, several 3D simulations using a 64^3 grid were run on a Xeon E5-4620 processor. For the compiler, we used `gcc` with the `-O3` option. For adiabatic HD, CRONOS achieves $7.34 \cdot 10^5$ and $6.65 \cdot 10^5$ cell updates per second using the HLL and the HLLC Riemann solver, respectively. For a similar setup the PLUTO code (Mignone et al. 2007, 2012) with the HLL Riemann solver achieves $6.1 \cdot 10^5$ cell updates per second. For adiabatic MHD using the HLLD solver together with a constrained-transport implementation as detailed in Gardiner & Stone (2005, 2008), CRONOS updates $2.5 \cdot 10^5$ cells per second, whereas PLUTO reaches $4.3 \cdot 10^5$ cell updates per second. Using the HLL Riemann solver, we also compared the perfor-

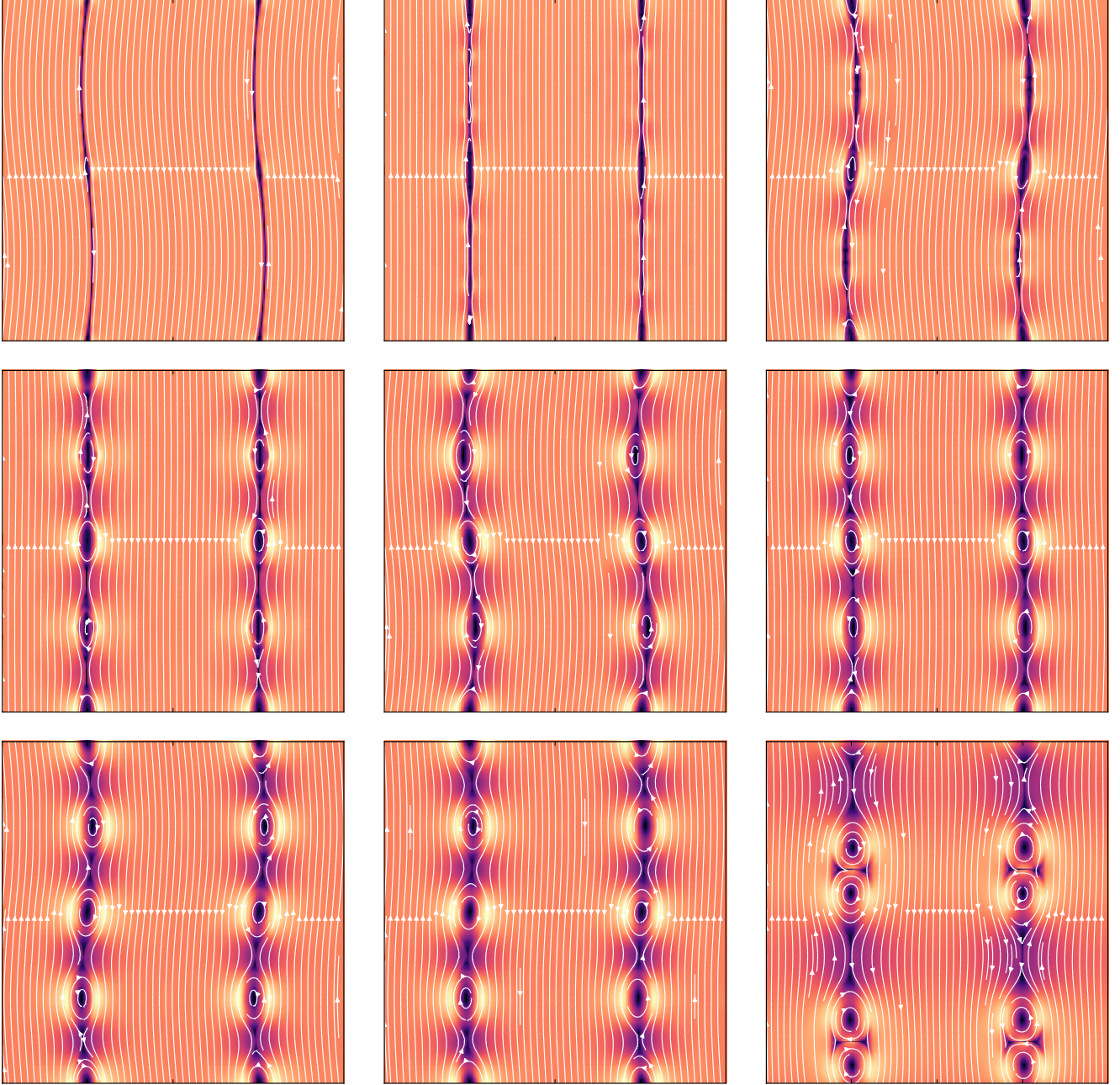


Figure 16. Magnetic field for the current-sheet test at times $t \in \{0.5, 1.0, 1.5, 2.0, 2.5, 3.0, 3.5, 4.0, 10.0\}$ (successively from upper left to lower right). The color indicates absolute magnetic field strength, with field lines (white) superimposed.

mance of the two different constrained-transport implementations employed within CRONOS. Using constrained transport based on cell-edge related electric fields with $2.6 \cdot 10^5$ cell updates per second is barely faster than the solution using the HLLD Riemann solver. Constrained transport based on face-centered fluxes in contrast reaches $3.3 \cdot 10^5$ cell updates per second.

It should be mentioned that, while PLUTO features operation modes that are specifically optimized for simulations on 1D and 2D grids, CRONOS currently treats any grid as 3D, leading to a computational overhead on low-dimensional problems. Correspondingly, PLUTO currently outperforms CRONOS for 1D and 2D problems.

9. EXTENSION: LOGICALLY RECTANGULAR GRIDS

Formerly, the available grid layouts in the CRONOS code were Cartesian, plane polar, and spherical, with the additional option to use an independent non-linear scaling in each dimension. Plane polar and spherical grids, however, suffer from grid singularities that can pose problems in given simulations setups. For example, if the interaction of a spherical outflow with a moving background medium is to be investigated, a spherical grid would be optimal for the outflow, but the singularity along the z -axis can lead to numerical problems there (but see the discussion in Ziegler 2011a). Additionally, cells near the z -axis become rather small, possibly leading to severe global time-step constraints.

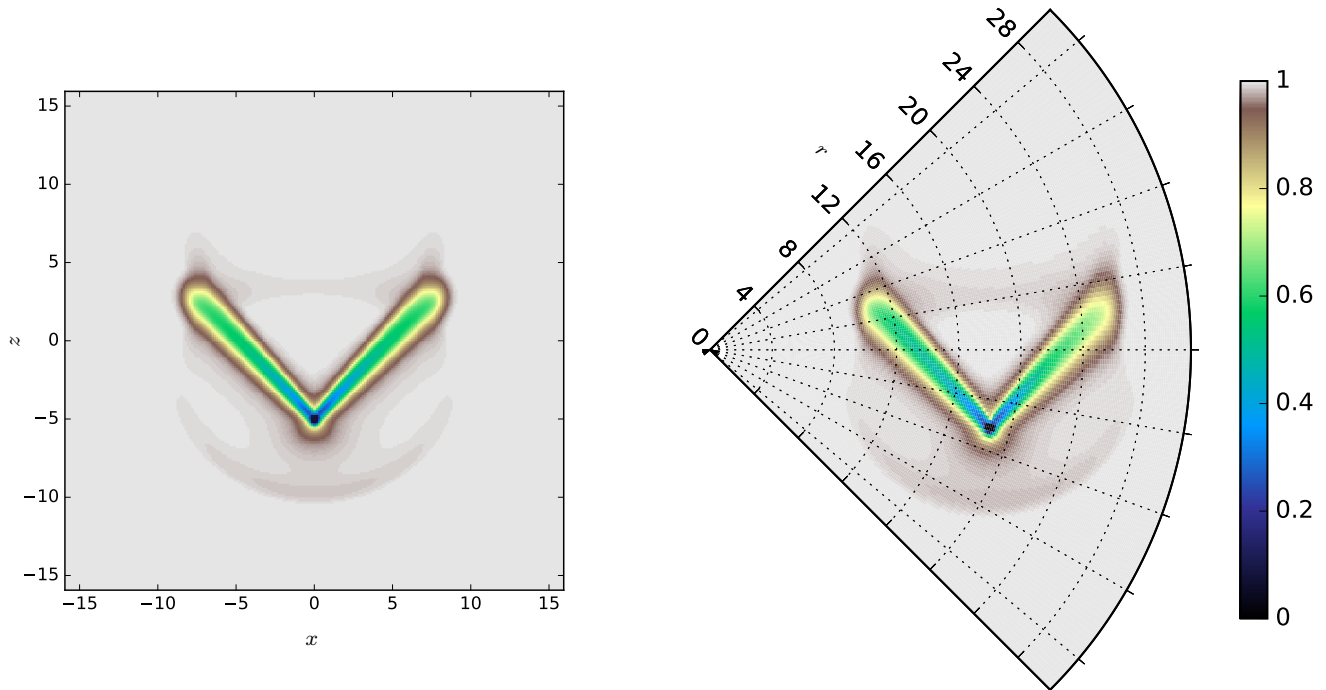


Figure 17. Contour plots for the absolute value of the velocity for the Alfvén wing test at time $t = 8$ in normalized units. Here, the x -direction is to the right and the z -direction to the top of the images. Results are shown for Cartesian (left) and spherical coordinates (right).

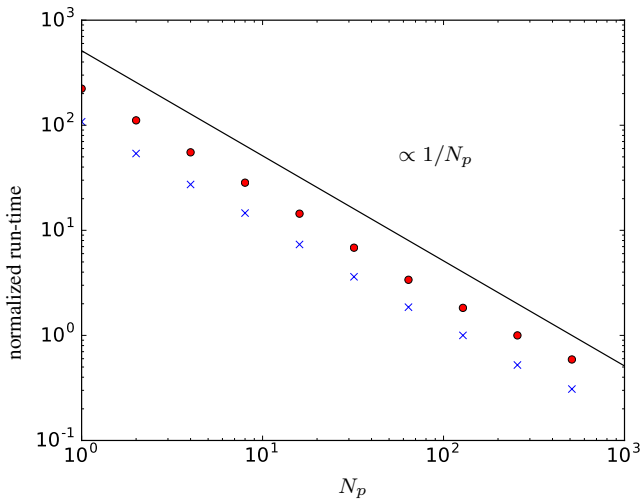


Figure 18. Normalized run-time of simulations carried out with CRONOS as a function of the number of used computing cores N_p for an HD (red circles) and an MHD (blue crosses) test case. Run times for the HD and MHD cases are normalized to those of 128 and 64 cores, respectively. The solid line indicates the dependence for perfect scaling.

Therefore, an additional type of grid has been implemented into CRONOS. The so-called logically rectangular grids are based on direct transformations of an underlying Cartesian grid into any desired geometry. Thus, the underlying grid management is still based on an orthogonal grid, motivating the term “logically rectangular” for this kind of grid. The general framework of such grids in the context of finite-volume methods is discussed in Calhoun et al. (2008), where a range of possible grid implementations is suggested and analyzed.

Here, the grid mapping from their Figure 3.2 (a) is used to run a blast-wave test on a 2D mesh. This mapping trans-

forms the Cartesian base grid onto a circular grid without any coordinate singularities. This grid mapping, however, is non-differentiable along the diagonal directions. Currently, results for the logically-rectangular-grid simulations are done using a piecewise constant reconstruction only, i.e., the code is spatially of first order in this case, with a second-order reconstruction still to be implemented.

The blast-wave test is initialized by injecting a localized high-pressure region into an otherwise homogeneous medium (Sedov 1959). Initially, we use a normalized density $n = 1$ and a normalized pressure $p = 10^{-5}$ everywhere in the numerical domain. Only in a small region of area A_{blast} (covering only a few cells) near the center, the thermal energy density e_{th} is increased via $e_{\text{th}} = E/A_{\text{blast}}$, where $E = 1$ is the total additional energy. The problem is solved both on a Cartesian grid and on a logically rectangular grid with unit radius.

Results for both grids are shown in Figure 19. Both recover the blast-wave problem to a similar degree. In most regions the logically rectangular grid is superior in reproducing the circular nature of the blast wave. This is particular evident from the intensity variation along a circle in the Cartesian case. Along the diagonal, however, the kink in the grid mapping leads to locally higher deviations. These are expected to reduce for a second-order reconstruction. Here, we note that the implementation of logically rectangular grids into the CRONOS framework is ongoing, where currently only HD simulations have been addressed so far.

10. SUMMARY

The CRONOS MHD code was developed for simulations in the context of astrophysics and space-physics studies. CRONOS uses a semi-discrete finite-volume scheme to ensure conservation of all relevant quantities. Thus, it is ideally suited for the treatment of high-Mach-number flows. The

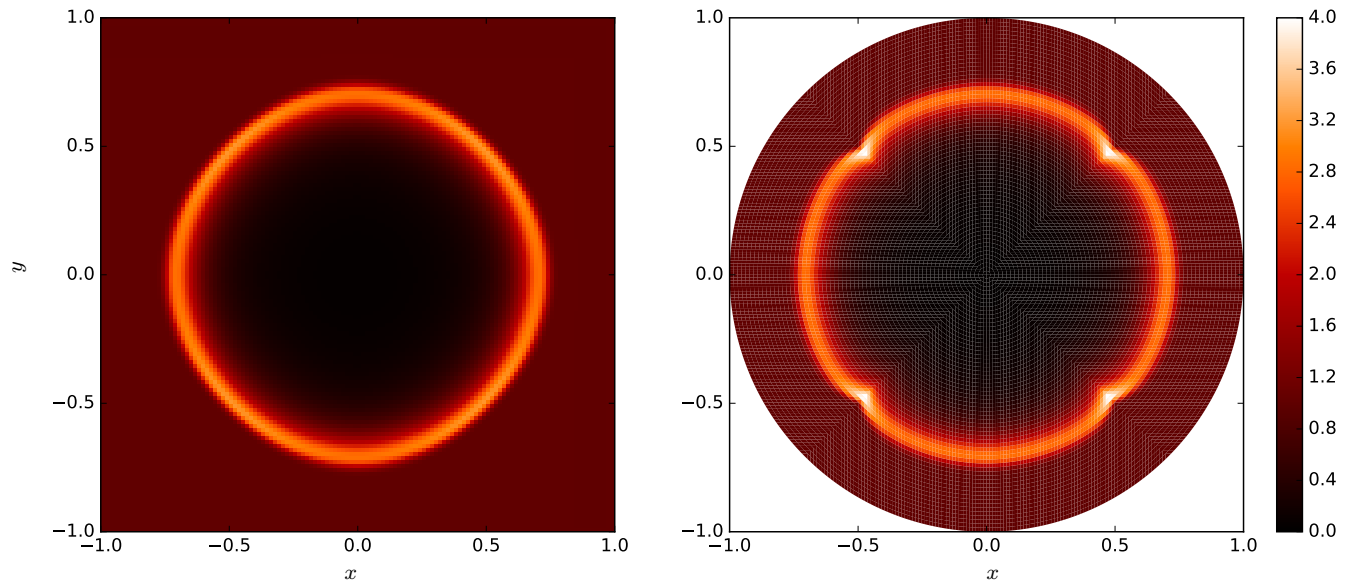


Figure 19. Simulation results for the Sedov-explosion test. Here, density at time $t = 0.5$ is shown for a Cartesian (left) and a logically rectangular grid (right).

code employs a second-order spatial reconstruction and can be used with a second- or third-order Runge–Kutta time integrator to advance the semi-discrete system of equations. Due to its high modularity, key features of the code can easily be extended or adapted. For example, adding further Riemann solvers or spatial reconstruction algorithms is fairly simple within the CRONOS framework. Apart from that, simulations are set up by implementing a user module describing the simulation setup. In the simplest case, only initial and boundary conditions need to be prescribed, while a broad range of additional options are foreseen.

Cartesian, plane-polar, and spherical grids are supported, where the grid in each orthogonal dimension can also be non-linear. Currently, logically rectangular grids are being implemented, where a first-order test was shown here.

Another feature setting CRONOS apart from most other codes is the option to solve the evolution equations for several fluids simultaneously. The equations for each fluid are solved independently from the others, leading to the same results as for a single-fluid simulation. Coupling of the different fluids can be introduced by the implementation of appropriate source terms by the user, thus allowing, e.g., the modeling of a fluid with a charged and a neutral phase. More generally, other types of (conservation) equations may be added and solved simultaneously, which is a useful property not only for passive tracers, but also for applications such as cosmic-ray propagation or the evolution of wave spectra. CRONOS is continuously enhanced to meet the needs of new scientific projects to be handled with the code. The CRONOS code is available upon request from the main author.

ACKNOWLEDGMENTS

We are grateful to Horst Fichtner and Klaus Scherer for valuable discussions and advice. This work was funded by the Austrian Science Fund (*Fonds zur Förderung der wissenschaftlichen Forschung, FWF*) through project I 1111-N27, as well as by the German Research Foundation (*Deutsche Forschungsgemeinschaft, DFG*) through project FI 706/15-1. Furthermore, J.K. acknowledges financial support through the *Ruhr Astroparticle and Plasma Physics (RAPP)*

Center, funded as MERCUR project St-2014-040. The computational results presented have been achieved in part using the HPC infrastructure of the University of Innsbruck.

REFERENCES

- Balsara, D. S. 1998, *ApJS*, 116, 133
 Balsara, D. S., & Spicer, D. 1999, *Journal of Computational Physics*, 148, 133
 Balsara, D. S., & Spicer, D. S. 1999, *J. Comp. Phys.*, 149, 270
 Biermann, L. 1951, *ZAp*, 29, 274
 Brackbill, J. U., & Barnes, D. C. 1980, *J. Comp. Phys.*, 35, 426
 Braginskii, S. I. 1965, *Reviews of Plasma Physics*, 1, 205
 Brio, M., & Wu, C. C. 1988, *J. Comp. Phys.*, 75, 400
 Calhoun, D. A., Helzel, C., & Leveque, R. J. 2008, *SIAM Review*, 50, 723
 Courant, R., Friedrichs, K., & Lewy, H. 1928, *Math. Ann.*, 100, 32
 Czechowski, A., & Kleimann, J. 2017, *Annales Geophysicae*, 35, 1033.
<https://www.ann-geophys.net/35/1033/2017/>
 Dalakishvili, G., Kleimann, J., Fichtner, H., & Poedts, S. 2011, *A&A*, 536, A100
 Dedner, A., Kemm, F., Kröner, D., et al. 2002, *J. Comp. Phys.*, 175, 645
 Dreher, J., & Grauer, R. 2005, *Parallel Computing*, 31, 913.
<https://doi.org/10.1016/j.parco.2005.04.011>
 Drell, S. D., Foley, H. M., & Ruderman, M. A. 1965, *J. Geophys. Res.*, 70, 3131
 Einfeldt, B., Roe, P. L., Munz, C. D., & Sjogreen, B. 1991, *Journal of Computational Physics*, 92, 273
 Evans, C. R., & Hawley, J. F. 1988, *ApJ*, 332, 659
 Flaig, M., Kissmann, R., & Kley, W. 2009, *MNRAS*, 394, 1887
 Flaig, M., Kley, W., & Kissmann, R. 2010, *MNRAS*, 409, 1297
 Flaig, M., Ruoff, P., Kley, W., & Kissmann, R. 2012, *MNRAS*, 420, 2419
 Fromang, S., Hennebelle, P., & Teyssier, R. 2006, *A&A*, 457, 371
 Gardiner, T. A., & Stone, J. M. 2005, *J. Comp. Phys.*, 205, 509
 —. 2008, *J. Comp. Phys.*, 227, 4123
 Godunov, S. K. 1959, *Mat. Sb.*, 47, 271
 Harten, A. 1983, *J. Comp. Phys.*, 49, 357
 Harten, A., Lax, P., & van Leer, B. 1983, *SIAM Review*, 25, 35
 Hawley, J. F., & Stone, J. M. 1995, *Computer Physics Communications*, 89, 127
 Hunter, J. D. 2007, *Computing In Science & Engineering*, 9, 90
 Keppens, R., Meliani, Z., van Marle, A. J., et al. 2012, *J. Comp. Phys.*, 231, 718
 Kissmann, R., Kleimann, J., Fichtner, H., & Grauer, R. 2008, *MNRAS*, 391, 1577
 Kissmann, R., & Pomoell, J. 2012, *SIAM J. Sci. Comput.*, 34, A763

- Kissmann, R., Reitberger, K., Reimer, O., Reimer, A., & Grimaldo, E. 2016, *ApJ*, 831, 121
- Kleimann, J., Kopp, A., Fichtner, H., & Grauer, R. 2009, *Annales Geophysicae*, 27, 989
- Kleimann, J., Röken, C., & Fichtner, H. 2017, *ApJ*, 838, 75
- Kopp, A., & Schröer, A. 1998, *Physica Scripta Volume T*, 74, 71
- Kurganov, A., Noelle, S., & Petrova, G. 2001, *SIAM J. Sci. Comput.*, 23, 707
- Kurganov, A., & Tadmor, E. 2000, *JCP*, 160, 241
- LeVeque, Randall, J. 2002, *Finite Volume Methods for Hyperbolic Problems* (Cambridge University Press)
- LeVeque, R. J. 2002, *Finite-Volume Methods for Hyperbolic Problems* (Cambridge University Press)
- Londrillo, P., & Del Zanna, L. 2000, *ApJ*, 530, 508
- . 2004, *J. Comp. Phys.*, 195, 17
- Mignone, A. 2007, *Journal of Computational Physics*, 225, 1427
- Mignone, A., Bodo, G., Massaglia, S., et al. 2007, *ApJS*, 170, 228
- Mignone, A., Zanni, C., Tzeferacos, P., et al. 2012, *ApJS*, 198, 7
- Miyoshi, T., & Kusano, K. 2005, *J. Comp. Phys.*, 208, 315
- Neubauer, F. M. 1980, *J. Geophys. Res.*, 85, 1171
- Orszag, S. A., & Tang, C.-M. 1979, *Journal of Fluid Mechanics*, 90, 129
- Osher, S. 1985, *SIAM Journal on Numerical Analysis*, 22, 947
- Pandolfi, M., & D'Ambrosio, D. 2001, *Journal of Computational Physics*, 166, 271
- Pareschi, L., Puppo, G., & Russo, G. 2005, *SIAM Journal on Scientific Computing*, 26, 979
- Parker, E. N. 1958, *ApJ*, 128, 664
- Quirk, J. J. 1994, *International Journal for Numerical Methods in Fluids*, 18, 555. <http://dx.doi.org/10.1002/flid.1650180603>
- Reitberger, K., Kissmann, R., Reimer, A., & Reimer, O. 2014a, *ApJ*, 789, 87
- Reitberger, K., Kissmann, R., Reimer, A., Reimer, O., & Dubus, G. 2014b, *ApJ*, 782, 96
- Ridley, A. J. 2007, *Annales Geophysicae*, 25, 533
- Roe, P. L. 1981, *J. Comp. Phys.*, 43, 357
- Roe, P. L. 1985, in *Large-Scale Computations in Fluid Mechanics*, ed. B. E. Engquist, S. Osher, & R. C. J. Somerville, 163–193
- Röken, C., Kleimann, J., & Fichtner, H. 2015, *ApJ*, 805, 173
- Ryu, D., & Goodman, J. 1994, *ApJ*, 422, 269
- Ryu, D., Jones, T. W., & Frank, A. 1995, *ApJ*, 452, 785
- Scherer, K., Fichtner, H., Jörg Fahr, H., Röken, C., & Kleimann, J. 2016a, *ApJ*, 833, 38
- Scherer, K., Fichtner, H., Kleimann, J., et al. 2016b, *A&A*, 586, A111
- Scherer, K., van der Schyff, A., Bomans, D. J., et al. 2015, *A&A*, 576, A97
- Sedov, L. I. 1959, *Similarity and Dimensional Methods in Mechanics* (Academic Press, New York)
- Shu, C.-W. 1988, *SIAM J. Sci. Stat. Comput.*, 9, 1073
- Shu, C.-W., & Osher, S. 1989, *J. Comp. Phys.*, 83, 32
- Skinner, M. A., & Ostriker, E. C. 2010, *ApJS*, 188, 290
- Sod, G. 1978, *J. Comp. Phys.*, 27, 1
- Stone, J. M., Gardiner, T. A., Teuben, P., Hawley, J. F., & Simon, J. B. 2008, *ApJS*, 178, 137
- Stone, J. M., & Norman, M. L. 1992a, *ApJS*, 80, 753
- . 1992b, *ApJS*, 80, 791
- Tóth, G. 2000, *J. Comp. Phys.*, 161, 605
- Teyssier, R. 2002, *A&A*, 385, 337
- Toro, E. F. 1997, *Riemann solvers and numerical methods for fluid dynamics : a practical introduction* (Berlin, New York: Springer)
- Toro, E. F., Spruce, M., & Speares, W. 1994, *Shock Waves*, 4, 25
- van der Holst, B., Keppens, R., & Meliani, Z. 2008, *Computer Physics Communications*, 179, 617
- van der Holst, B., Keppens, R., Meliani, Z., et al. 2012, *MPI-AMRVAC: MPI-Adaptive Mesh Refinement-Versatile Advection Code*, , , astrophysics Source Code Library, ascl:1208.014
- van Leer, B. 1977, *J. Comp. Phys.*, 23, 276
- . 1979, *J. Comp. Phys.*, 32, 101
- Wiengarten, T., Fichtner, H., Kleimann, J., & Kissmann, R. 2015, *ApJ*, 805, 155
- Wiengarten, T., Kleimann, J., Fichtner, H., et al. 2013, *Journal of Geophysical Research (Space Physics)*, 118, 29
- . 2014, *ApJ*, 788, 80
- Wiengarten, T., Oughton, S., Engelbrecht, N. E., et al. 2016, *ApJ*, 833, 17
- Wisniewski, M., Spanier, F., & Kissmann, R. 2012, *ApJ*, 750, 150
- Zaqarashvili, T. V., Khodachenko, M. L., & Rucker, H. O. 2011, *A&A*, 529, A82
- Ziegler, U. 2004, *J. Comp. Phys.*, 196, 393
- . 2008, *Computer Physics Communications*, 179, 227
- . 2011a, *J. Comp. Phys.*, 230, 1035
- . 2011b, *NIRVANA: A Numerical Tool for Astrophysical Gas Dynamics*, , astrophysics Source Code Library, ascl:1101.006